

Longitudinal double-spin asymmetry for inclusive jet and dijet production in pp collisions at $\sqrt{s} = 510$ GeV

J. Adam,⁶ L. Adamczyk,² J. R. Adams,³⁹ J. K. Adkins,³⁰ G. Agakishiev,²⁸ M. M. Aggarwal,⁴⁰ Z. Ahammed,⁶⁰ I. Alekseev,^{3,35} D. M. Anderson,⁵⁴ R. Aoyama,⁵⁷ A. Aparin,²⁸ D. Arkhipkin,⁶ E. C. Aschenauer,⁶ M. U. Ashraf,⁵⁶ F. Atetalla,²⁹ A. Attri,⁴⁰ G. S. Averichev,²⁸ V. Bairathi,³⁶ K. Barish,¹⁰ A. J. Bassill,¹⁰ A. Behera,⁵² R. Bellwied,²⁰ A. Bhasin,²⁷ A. K. Bhati,⁴⁰ J. Bielcik,¹⁴ J. Bielcikova,³⁸ L. C. Bland,⁶ I. G. Bordyuzhin,³ J. D. Brandenburg,^{49,6} A. V. Brandin,³⁵ J. Bryslawskyj,¹⁰ I. Bunzarov,²⁸ J. Butterworth,⁴⁵ H. Caines,⁶³ M. Calderón de la Barca Sánchez,⁸ D. Cebra,⁸ I. Chakaberia,^{29,6} P. Chaloupka,¹⁴ B. K. Chan,⁹ F.-H. Chang,³⁷ Z. Chang,⁶ N. Chankova-Bunzarova,²⁸ A. Chatterjee,⁶⁰ S. Chattopadhyay,⁶⁰ J. H. Chen,¹⁸ X. Chen,⁴⁸ J. Cheng,⁵⁶ M. Cherney,¹³ W. Christie,⁶ H. J. Crawford,⁷ M. Csanád,¹⁶ S. Das,¹¹ T. G. Dedovich,²⁸ I. M. Deppner,¹⁹ A. A. Derevschikov,⁴² L. Didenko,⁶ C. Dilks,⁴¹ X. Dong,³¹ J. L. Drachenberg,¹ J. C. Dunlop,⁶ T. Edmonds,⁴³ N. Elsey,⁶² J. Engelage,⁷ G. Eppley,⁴⁵ R. Esha,⁵² S. Esumi,⁵⁷ O. Evdokimov,¹² J. Ewigleben,³² O. Eyser,⁶ R. Fatemi,³⁰ S. Fazio,⁶ P. Federic,³⁸ J. Fedorisin,²⁸ Y. Feng,⁴³ P. Filip,²⁸ E. Finch,⁵¹ Y. Fisyak,⁶ L. Fulek,² C. A. Gagliardi,⁵⁴ T. Galatyuk,¹⁵ F. Geurts,⁴⁵ A. Gibson,⁵⁹ K. Gopal,²³ D. Grosnick,⁵⁹ A. Gupta,²⁷ W. Gurny,⁶ A. I. Hamad,²⁹ A. Hamed,⁵ J. W. Harris,⁶³ L. He,⁴³ S. Heppelmann,⁸ S. Heppelmann,⁴¹ N. Herrmann,¹⁹ L. Holub,¹⁴ Y. Hong,³¹ S. Horvat,⁶³ B. Huang,¹² H. Z. Huang,⁹ S. L. Huang,⁵² T. Huang,³⁷ X. Huang,⁵⁶ T. J. Humanic,³⁹ P. Huo,⁵² G. Igo,⁹ W. W. Jacobs,²⁵ C. Jena,²³ A. Jentsch,⁶ Y. Ji,⁴⁸ J. Jia,^{6,52} K. Jiang,⁴⁸ S. Jowzaee,⁶² X. Ju,⁴⁸ E. G. Judd,⁷ S. Kabana,²⁹ S. Kagamaster,³² D. Kalinkin,²⁵ K. Kang,⁵⁶ D. Kapukchyan,¹⁰ K. Kauder,⁶ H. W. Ke,⁶ D. Keane,²⁹ A. Kechechyan,²⁸ M. Kelsey,³¹ Y. V. Khyzhniak,³⁵ D. P. Kikoła,⁶¹ C. Kim,¹⁰ T. A. Kinghorn,⁸ I. Kisel,¹⁷ A. Kisiel,⁶¹ M. Kocan,¹⁴ L. Kochenda,³⁵ L. K. Kosarzewski,¹⁴ L. Kramarik,¹⁴ P. Kravtsov,³⁵ K. Krueger,⁴ N. Kulathunga Mudiyansele,²⁰ L. Kumar,⁴⁰ R. Kunnawalkam Elayavalli,⁶² J. H. Kwasizur,²⁵ R. Lacey,⁵² J. M. Landgraf,⁶ J. Lauret,⁶ A. Lebedev,⁶ R. Lednicky,²⁸ J. H. Lee,⁶ C. Li,⁴⁸ W. Li,⁵⁰ W. Li,⁴⁵ X. Li,⁴⁸ Y. Li,⁵⁶ Y. Liang,²⁹ R. Licenik,³⁸ T. Lin,⁵⁴ A. Lipiec,⁶¹ M. A. Lisa,³⁹ F. Liu,¹¹ H. Liu,²⁵ P. Liu,⁵² P. Liu,⁵⁰ T. Liu,⁶³ X. Liu,³⁹ Y. Liu,⁵⁴ Z. Liu,⁴⁸ T. Ljubicic,⁶ W. J. Llope,⁶² M. Lomnitz,³¹ R. S. Longacre,⁶ S. Luo,¹² X. Luo,¹¹ G. L. Ma,⁵⁰ L. Ma,¹⁸ R. Ma,⁶ Y. G. Ma,⁵⁰ N. Magdy,¹² R. Majka,⁶³ D. Mallick,³⁶ S. Margetis,²⁹ C. Markert,⁵⁵ H. S. Matis,³¹ O. Matonoha,¹⁴ J. A. Mazer,⁴⁶ K. Meehan,⁸ J. C. Mei,⁴⁹ N. G. Minaev,⁴² S. Mioduszewski,⁵⁴ D. Mishra,³⁶ B. Mohanty,³⁶ M. M. Mondal,²⁶ I. Mooney,⁶² Z. Moravcova,¹⁴ D. A. Morozov,⁴² Md. Nasim,²² K. Nayak,¹¹ J. M. Nelson,⁷ D. B. Nemes,⁶³ M. Nie,⁴⁹ G. Nigmatkulov,³⁵ T. Niida,⁶² L. V. Nogach,⁴² T. Nonaka,¹¹ G. Odyniec,³¹ A. Ogawa,⁶ K. Oh,⁴⁴ S. Oh,⁶³ V. A. Okorokov,³⁵ B. S. Page,⁶ R. Pak,⁶ Y. Panebratsev,²⁸ B. Pawlik,² D. Pawłowska,⁶¹ H. Pei,¹¹ C. Perkins,⁷ R. L. Pintér,¹⁶ J. Pluta,⁶¹ J. Porter,³¹ M. Posik,⁵³ N. K. Pruthi,⁴⁰ M. Przybycien,² J. Putschke,⁶² A. Quintero,⁵³ S. K. Radhakrishnan,³¹ S. Ramachandran,³⁰ R. L. Ray,⁵⁵ R. Reed,³² H. G. Ritter,³¹ J. B. Roberts,⁴⁵ O. V. Rogachevskiy,²⁸ J. L. Romero,⁸ L. Ruan,⁶ J. Rusnak,³⁸ O. Rusnakova,¹⁴ N. R. Sahoo,⁴⁹ P. K. Sahu,²⁶ S. Salur,⁴⁶ J. Sandweiss,⁶³ J. Schambach,⁵⁵ W. B. Schmidke,⁶ N. Schmitz,³³ B. R. Schweid,⁵² F. Seck,¹⁵ J. Seger,¹³ M. Sergeeva,⁹ R. Seto,¹⁰ P. Seyboth,³³ N. Shah,²⁴ E. Shahaliev,²⁸ P. V. Shanmuganathan,³² M. Shao,⁴⁸ F. Shen,⁴⁹ W. Q. Shen,⁵⁰ S. S. Shi,¹¹ Q. Y. Shou,⁵⁰ E. P. Sichtermann,³¹ S. Siejka,⁶¹ R. Sikora,² M. Simko,³⁸ J. Singh,⁴⁰ S. Singha,²⁹ D. Smirnov,⁶ N. Smirnov,⁶³ W. Solyst,²⁵ P. Sorensen,⁶ H. M. Spinka,⁴ B. Srivastava,⁴³ T. D. S. Stanislaus,⁵⁹ M. Stefaniak,⁶¹ D. J. Stewart,⁶³ M. Strikhanov,³⁵ B. Stringfellow,⁴³ A. A. P. Suaide,⁴⁷ T. Sugiura,⁵⁷ M. Sumner,³⁸ B. Summa,⁴¹ X. M. Sun,¹¹ Y. Sun,⁴⁸ Y. Sun,²¹ B. Surrow,⁵³ D. N. Svirida,³ P. Szymanski,⁶¹ A. H. Tang,⁶ Z. Tang,⁴⁸ A. Taranenko,³⁵ T. Tarnowsky,³⁴ J. H. Thomas,³¹ A. R. Timmins,²⁰ D. Tlusty,¹³ T. Todoroki,⁶ M. Tokarev,²⁸ C. A. Tomkiel,³² S. Trentalange,⁹ R. E. Tribble,⁵⁴ P. Tribedy,⁶ S. K. Tripathy,²⁶ O. D. Tsai,⁹ B. Tu,¹¹ Z. Tu,⁶ T. Ullrich,⁶ D. G. Underwood,⁴ I. Upsal,^{49,6} G. Van Buren,⁶ J. Vanek,³⁸ A. N. Vasiliev,⁴² I. Vassiliev,¹⁷ F. Videbæk,⁶ S. Vokal,²⁸ S. A. Voloshin,⁶² F. Wang,⁴³ G. Wang,⁹ P. Wang,⁴⁸ Y. Wang,¹¹ Y. Wang,⁵⁶ J. C. Webb,⁶ L. Wen,⁹ G. D. Westfall,³⁴ H. Wieman,³¹ S. W. Wissink,²⁵ R. Witt,⁵⁸ Y. Wu,²⁹ Z. G. Xiao,⁵⁶ G. Xie,¹² W. Xie,⁴³ H. Xu,²¹ N. Xu,³¹ Q. H. Xu,⁴⁹ Y. F. Xu,⁵⁰ Z. Xu,⁶ C. Yang,⁴⁹ Q. Yang,⁴⁹ S. Yang,⁶ Y. Yang,³⁷ Z. Yang,¹¹ Z. Ye,⁴⁵ Z. Ye,¹² L. Yi,⁴⁹ K. Yip,⁶ I.-K. Yoo,⁴⁴ H. Zbroszczyk,⁶¹ W. Zha,⁴⁸ D. Zhang,¹¹ L. Zhang,¹¹ S. Zhang,⁴⁸ S. Zhang,⁵⁰ X. P. Zhang,⁵⁶ Y. Zhang,⁴⁸ Z. Zhang,⁵⁰ J. Zhao,⁴³ C. Zhong,⁵⁰ C. Zhou,⁵⁰ X. Zhu,⁵⁶ Z. Zhu,⁴⁹ M. Zurek,³¹ and M. Zyzak¹⁷

(STAR Collaboration)

¹Abilene Christian University, Abilene, Texas 79699²AGH University of Science and Technology, FPACS, Cracow 30-059, Poland³Alikhanov Institute for Theoretical and Experimental Physics, Moscow 117218, Russia⁴Argonne National Laboratory, Argonne, Illinois 60439

- ⁵American Univerisity of Cairo, Cairo, Egypt
- ⁶Brookhaven National Laboratory, Upton, New York 11973
- ⁷University of California, Berkeley, California 94720
- ⁸University of California, Davis, California 95616
- ⁹University of California, Los Angeles, California 90095
- ¹⁰University of California, Riverside, California 92521
- ¹¹Central China Normal University, Wuhan, Hubei 430079
- ¹²University of Illinois at Chicago, Chicago, Illinois 60607
- ¹³Creighton University, Omaha, Nebraska 68178
- ¹⁴Czech Technical University in Prague, FNSPE, Prague 115 19, Czech Republic
- ¹⁵Technische Universität Darmstadt, Darmstadt 64289, Germany
- ¹⁶Eötvös Loránd University, Budapest, Hungary H-1117
- ¹⁷Frankfurt Institute for Advanced Studies FIAS, Frankfurt 60438, Germany
- ¹⁸Fudan University, Shanghai, 200433
- ¹⁹University of Heidelberg, Heidelberg 69120, Germany
- ²⁰University of Houston, Houston, Texas 77204
- ²¹Huzhou University, Huzhou, Zhejiang 313000
- ²²Indian Institute of Science Education and Research (IISER), Berhampur 760010, India
- ²³Indian Institute of Science Education and Research, Tirupati 517507, India
- ²⁴Indian Institute Technology, Patna, Bihar, India
- ²⁵Indiana University, Bloomington, Indiana 47408
- ²⁶Institute of Physics, Bhubaneswar 751005, India
- ²⁷University of Jammu, Jammu 180001, India
- ²⁸Joint Institute for Nuclear Research, Dubna 141 980, Russia
- ²⁹Kent State University, Kent, Ohio 44242
- ³⁰University of Kentucky, Lexington, Kentucky 40506-0055
- ³¹Lawrence Berkeley National Laboratory, Berkeley, California 94720
- ³²Lehigh University, Bethlehem, Pennsylvania 18015
- ³³Max-Planck-Institut für Physik, Munich 80805, Germany
- ³⁴Michigan State University, East Lansing, Michigan 48824
- ³⁵National Research Nuclear University MEPhI, Moscow 115409, Russia
- ³⁶National Institute of Science Education and Research, HBNI, Jatni 752050, India
- ³⁷National Cheng Kung University, Tainan 70101
- ³⁸Nuclear Physics Institute of the CAS, Rez 250 68, Czech Republic
- ³⁹Ohio State University, Columbus, Ohio 43210
- ⁴⁰Panjab University, Chandigarh 160014, India
- ⁴¹Pennsylvania State University, University Park, Pennsylvania 16802
- ⁴²NRC “Kurchatov Institute”, Institute of High Energy Physics, Protvino 142281, Russia
- ⁴³Purdue University, West Lafayette, Indiana 47907
- ⁴⁴Pusan National University, Pusan 46241, Korea
- ⁴⁵Rice University, Houston, Texas 77251
- ⁴⁶Rutgers University, Piscataway, New Jersey 08854
- ⁴⁷Universidade de São Paulo, São Paulo, Brazil 05314-970
- ⁴⁸University of Science and Technology of China, Hefei, Anhui 230026
- ⁴⁹Shandong University, Qingdao, Shandong 266237
- ⁵⁰Shanghai Institute of Applied Physics, Chinese Academy of Sciences, Shanghai 201800
- ⁵¹Southern Connecticut State University, New Haven, Connecticut 06515
- ⁵²State University of New York, Stony Brook, New York 11794
- ⁵³Temple University, Philadelphia, Pennsylvania 19122
- ⁵⁴Texas A&M University, College Station, Texas 77843
- ⁵⁵University of Texas, Austin, Texas 78712
- ⁵⁶Tsinghua University, Beijing 100084
- ⁵⁷University of Tsukuba, Tsukuba, Ibaraki 305-8571, Japan
- ⁵⁸United States Naval Academy, Annapolis, Maryland 21402
- ⁵⁹Valparaiso University, Valparaiso, Indiana 46383
- ⁶⁰Variable Energy Cyclotron Centre, Kolkata 700064, India
- ⁶¹Warsaw University of Technology, Warsaw 00-661, Poland
- ⁶²Wayne State University, Detroit, Michigan 48201
- ⁶³Yale University, New Haven, Connecticut 06520



(Received 9 June 2019; published 9 September 2019)

We report the first measurement of the inclusive jet and the dijet longitudinal double-spin asymmetries, A_{LL} , at midrapidity in polarized pp collisions at a center-of-mass energy $\sqrt{s} = 510$ GeV. The inclusive jet A_{LL} measurement is sensitive to the gluon helicity distribution down to a gluon momentum fraction of $x \approx 0.015$, while the dijet measurements, separated into four jet-pair topologies, provide constraints on the x dependence of the gluon polarization. Both results are consistent with previous measurements made at $\sqrt{s} = 200$ GeV in the overlapping kinematic region, $x > 0.05$, and show good agreement with predictions from recent next-to-leading order global analyses.

DOI: [10.1103/PhysRevD.100.052005](https://doi.org/10.1103/PhysRevD.100.052005)

I. INTRODUCTION

The proton consists of quarks and antiquarks, bound by gluons. The gluons provide about half of the momentum of the proton (see e.g., [1]), and their interactions provide most of the mass [2,3]. Nonetheless, we know very little about the role that gluons play in determining the fundamental proton quantum numbers, such as its spin.

The spin program at the Relativistic Heavy Ion Collider (RHIC) has made significant progress toward addressing the question of how much, if at all, gluon spins contribute to the spin of the proton. The STAR and PHENIX collaborations have performed a sequence of measurements of the longitudinal double-spin asymmetry, A_{LL} , for inclusive jet [4–7] and pion [8–12] production. The results have been incorporated, along with inclusive and semi-inclusive lepton-proton scattering data, into the recent DSSV14 [13] and NNPDFpol1.1 [14] next-to-leading order (NLO) perturbative QCD global analyses. These extractions of the helicity parton distribution functions (PDFs) indicate that, at momentum transfer scale of $Q^2 = 10$ (GeV/c)² and for momentum fractions $x > 0.05$ that are sampled by the included RHIC data, gluon spins contribute approximately 40% of the total proton spin.

RHIC data provide direct, leading-order sensitivity to gluon polarization because hard scattering processes at RHIC energies are dominated by gluon-gluon and quark-gluon scattering, as shown in Fig. 1. In contrast, polarized lepton scattering data constrain the gluon polarization indirectly, via Q^2 evolution effects. There have been two recent global analyses [15,16] that only included lepton scattering data in their fits. These fits also find substantial gluon polarization in the region $x > 0.05$, albeit with larger uncertainties than those of [13,14]. Recently, the first lattice QCD calculation of the full first moment of the gluon helicity distribution $\Delta g(x, Q^2)$ has been calculated to

be $\Delta G(Q^2) = \int_0^1 \Delta g(x, Q^2) dx = 0.251 \pm 0.047(\text{stat.}) \pm 0.016(\text{syst.})$ at $Q^2 = 10$ (GeV/c)² [17]. In addition, the small- x asymptotic behavior of $\Delta g(x)$ has been derived in the large- N_c limit [18], although the x range where the asymptotic limit is applicable is not yet clear.

While the DSSV14 and NNPDFpol1.1 analyses are in good agreement for the kinematic region $x > 0.05$ where the included data from RHIC on inclusive jet and neutral pion production at $\sqrt{s} = 200$ GeV are most sensitive, the extrapolations over smaller x and their associated errors are markedly different. For example, at $x = 10^{-3}$, the quoted gluon polarization uncertainty in NNPDFpol1.1 is twice as large as that for DSSV14. These extrapolations are needed to determine the full first moment of the gluon helicity distribution. Complementary measurements are thus required both to extend the sensitivity to smaller x and better to resolve the x dependence of $\Delta g(x, Q^2)$.

The inclusive jet and the dijet longitudinal double-spin asymmetries presented in this paper will help address both issues. The data for these measurements were collected from $\sqrt{s} = 510$ GeV polarized pp collisions during the 2012 RHIC running period. For a given jet transverse momentum, p_T , and pseudorapidity, η , the increased

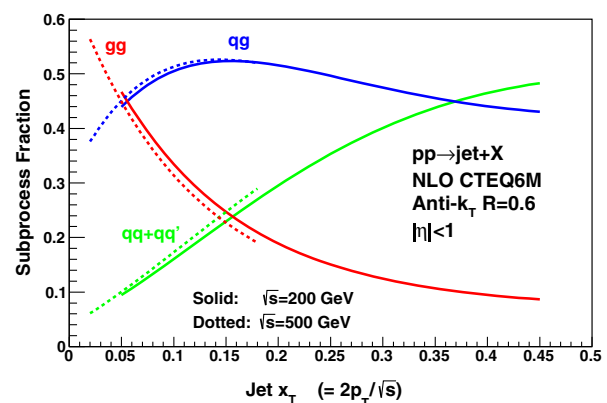


FIG. 1. Fractions of the next-to-leading-order cross section [19,20] for inclusive jet production arising from quark-quark, quark-gluon, and gluon-gluon scattering in pp collisions at $\sqrt{s} = 200$ and 500 GeV, as a function of $x_T = 2p_T/\sqrt{s}$.

center-of-mass energy extends the sensitivity of the inclusive jet channel to lower x partons ($x \simeq x_T e^{\pm\eta}$, where $x_T = 2p_T/\sqrt{s}$). While the inclusive jet channel provides the strongest statistical power, dijets permit extraction of the momentum fractions, $x_1 = (p_{T,3}e^{+\eta_3} + p_{T,4}e^{+\eta_4})/\sqrt{s}$ and $x_2 = (p_{T,3}e^{-\eta_3} + p_{T,4}e^{-\eta_4})/\sqrt{s}$, of the partons participating in the hard scattering at the Born level, with higher-order corrections that are known and have been shown to be small [21]. Note that, throughout this paper, the kinematics of the initial partons and final jets are denoted by subscripts 1,2 and 3,4, respectively. The $\sqrt{s} = 510$ GeV dijet asymmetries here are separated into four pseudorapidity topologies that facilitate the extraction of x -dependent constraints as a function of the dijet invariant mass $M_{34} = \sqrt{s x_1 x_2}$. Together, these inclusive jet and dijet results will provide important new constraints on the magnitude and shape of the gluon polarization over the range $0.015 < x < 0.2$.

A number of other measurements sensitive to gluon polarization have been released since the DSSV14 and NNPDFpol1.1 global analyses. STAR has published the first two measurements of dijet A_{LL} , based on pp collision data at $\sqrt{s} = 200$ GeV. One measurement considers asymmetries for dijets at midrapidity [22], while the second considers cases where at least one jet falls within $0.8 < \eta < 1.8$ [23]. Very recently, an update of the DSSV14 fit has been performed that includes these two dijet measurements by reweighting [24]. The updated fit finds that inclusion of the STAR $\sqrt{s} = 200$ GeV dijet results leads to a small increase in the size of $\Delta g(x)$ in the region $0.05 < x < 0.2$, together with a sizable reduction in the width of the uncertainty band, with the latter most notable in the region $x \gtrsim 0.2$.

Asymmetries have also been measured for inclusive π^0 production in 510 GeV pp collisions at $|\eta| < 0.35$ by PHENIX [25] and at $2.65 < \eta < 3.9$ by STAR [26]. These π^0 asymmetries provide sensitivity to gluon polarization down to $x \approx 0.01$ and $x \approx 0.001$, respectively.

The remainder of this paper is organized as follows. Section II briefly describes the components of the RHIC complex and the Solenoidal Tracker at RHIC (STAR) detector that are relevant to this measurement. Section III discusses jet reconstruction, including an underlying event and background subtraction technique. Section IV reviews the simulation sample that is used to correct the data for detector effects such as acceptance and resolution and to estimate systematic uncertainty contributions. Section V discusses the determination of A_{LL} and contributions to the systematic uncertainty. Section VI presents the results, along with comparisons to theoretical predictions. Section VII provides a brief conclusion.

II. EXPERIMENT AND DATA

A. The STAR detector at RHIC

The RHIC complex has accelerated and collided beams of polarized protons at center-of-mass energies ranging

from 62–510 GeV [27–29]. During the 2012 running period, each beam was typically filled with 111 bunches of vertically polarized protons. Rotator magnets placed on either side of the STAR interaction region were used to rotate the proton spin orientation from vertical to longitudinal. To minimize systematic effects due to bunch-to-bunch variations, the helicity state assigned to a pair of colliding bunches ($++$, $+-$, $-+$, $--$) was varied through the 2012 running period. This design also allowed for the flipping of beam spin orientation at the same rate as the colliding bunches, on the order of once every 100 ns. For a given storage period, or fill, the polarization of each beam was measured several times using Coulomb-nuclear interference (CNI) proton-carbon polarimeters [30]. The CNI polarimeters were calibrated with a polarized atomic hydrogen gas-jet target [31]. The luminosity-weighted polarizations for the two beams, which are referred to as “blue” and “yellow,” were 54% and 55%.

STAR is a large acceptance, multipurpose detector located at the RHIC 6 o’clock interaction region [32]. The detector components used in this analysis are the time projection chamber (TPC), the barrel (BEMC) and endcap (EEMC) electromagnetic calorimeters (collectively, EMCs), the vertex position detector (VPD), and the zero degree calorimeters (ZDC). The TPC measures the momentum of charged particles scattered within $|\eta| \lesssim 1.3$ and $0 < \phi < 2\pi$ [33]. The EMCs measure the energy of photons, electrons, and positrons, and provide the triggering. The BEMC [34] spans the region $-1 < \eta < 1$, and the EEMC [35] spans $1.1 < \eta < 2$, both with full azimuth. The VPD and ZDC are pairs of far-forward, fast-response detectors east and west of the interaction region. The VPD samples the region $4.2 < |\eta| < 5.2$ [36], while the ZDCs cover $|\eta| > 6.6$ [37]. Hit information from the VPD and ZDC detectors is used to extract the relative luminosities of the colliding bunches associated with a given helicity state. Azimuthal segmentation in the ZDC also allows it to serve as a local polarimeter to verify that the rotator magnets are set and functioning properly.

B. Triggers and event selection

STAR sampled 82 pb⁻¹ of longitudinally polarized pp collisions at $\sqrt{s} = 510$ GeV during the 2012 running period. The inclusive jet and the dijet analyses both utilize jet patch (JP) triggers which are constructed by applying thresholds to the total transverse energy (E_T) detected within $\Delta\eta \times \Delta\phi = 1 \times 1$ regions in the EMCs. There are a total of 30 jet patches, with five patches that overlap in η for each of six nonoverlapping regions in ϕ . An event satisfied the JP0, JP1 or JP2 trigger if the E_T of at least one of the jet patches exceeded 5.4, 7.3 or 14.4 GeV, respectively. All JP2-triggered events were recorded while the JP0 and JP1 triggers were prescaled to fit within the available data-acquisition bandwidth. During off-line processing, events are also required to pass a software trigger simulator that

incorporates time-dependent pedestal variations and detector efficiencies.

Candidate collision vertices are reconstructed from TPC tracks and hits in the EMCs and then ranked based on the number of in-time tracks and their transverse momenta. To ensure reasonable detector acceptance and minimize pileup events, only the highest quality vertex in each event is selected, and the position along the beam line, z_{vertex} , is required to fall within ± 90 cm of the center of the STAR detector.

The vertex reconstruction efficiency drops rapidly at the highest instantaneous luminosities achieved during the 2012 running period. The highest luminosity data are excluded from the inclusive jet analysis in order to minimize errors due to associating jets with the wrong vertex, as discussed in Sec. V D 3. In contrast, these data are included in the dijet analysis, as the higher observed track multiplicity makes it much less likely to assign the wrong vertex to a dijet event.

III. JET RECONSTRUCTION

A jet is a cluster of particles that originates from fragmentation and hadronization of an energetic final-state parton in a hard scattering process. They are abundantly produced at RHIC in $2 \rightarrow 2$ QCD processes where an initial-state parton is freed from a polarized proton beam. At STAR, jets are reconstructed from the charged tracks measured by the TPC and the energy deposits in the EMCs. The STAR jet finding algorithms have evolved in step with advances of jet finding techniques in the community and with the increasingly complex experimental conditions that accompany higher center-of-mass energy collisions and luminosities. Early STAR pp analyses [4–6] implemented the mid-point cone algorithm [38]. The cone radius varied from $R = 0.4$ – 0.7 as the EMCs acceptance was gradually expanded. The 2009 $\sqrt{s} = 200$ GeV inclusive jet analysis [7] represented the first STAR results obtained with the anti- k_T algorithm [39], a change that significantly reduces the sensitivity to soft background and pileup effects. The inclusive jet and dijet analyses presented in this paper also use the anti- k_T algorithm, as implemented in FASTJET version 3.0.6 [40], but with a smaller jet resolution parameter, $R = 0.5$ vs $R = 0.6$ at $\sqrt{s} = 200$ GeV, to reduce the increased contributions from soft background at $\sqrt{s} = 510$ GeV.

A. Inputs to the jet finder

The TPC tracks included in the jet finding algorithm are required to have at least 12 fit points out of a possible 45 to provide good momentum resolution. To remove split tracks, the number of hit points must be greater than 51% of the maximum possible number when the track geometry and active electronic channels are considered. In addition, tracks must have transverse momenta $p_T > 0.2$ GeV/ c and be associated with the selected vertex

for the event within a p_T -dependent distance of closest approach (DCA). The DCA is required to be less than 2 cm for $p_T < 0.5$ GeV/ c and less than 1 cm for $p_T > 1.5$ GeV/ c ; the DCA requirement is linearly interpolated between these two limits. The four-momenta of the charged tracks are constructed by equating the rest mass of each track to the pion mass. The EMC tower hits included in the jet finding algorithm are required to have a signal well above pedestal and an $E_T > 0.2$ GeV. The 4-momentum of an EMC hit is constructed by setting the rest mass to zero, as if all the energy deposited was due to photons originating from the vertex.

For tracks pointing to an EMC hit, the track p_T (multiplied by c to account for units) is subtracted from the tower E_T . If the difference is less than zero, the tower is discarded from the jet finding. This procedure, which is referred to as “ p_T subtraction,” avoids double counting from electrons and positrons that are fully reconstructed by both the TPC and EMCs. In contrast, on average charged hadrons deposit only $\simeq 30\%$ of their energy in the EMC material. Therefore, p_T subtraction results in an over-subtraction in the rare case where a photon strikes the same tower as a charged hadron. However, by suppressing the sensitivity to the large event-to-event fluctuations in the charged hadron energy deposition, it significantly improves the resolution of the reconstructed jet energy [7].

B. Underlying event subtraction

The underlying event (UE) is composed of low- p_T particles originating from multiple parton interactions and soft interactions between the scattered partons and proton remnants. The underlying event at RHIC energies is expected to be isotropic and approximately independent of the scale of the hard interaction [41]. As a result, distortions to the energy scale are largest for low- p_T jets. The UE has also been assumed to be spin independent [7], but that assumption has not been verified experimentally before this work.

A technique, adapted from the ALICE experiment [42], is applied for each jet in the analysis to correct the underlying event contribution to the reconstructed jet p_T and dijet invariant mass M_{inv} . The algorithm, called the off-axis method, scans the same list of TPC tracks and EMC hits that was input to the jet finder and selects those located in two off-axis cones, with radius $R = 0.5$ (chosen to match the anti- k_T resolution parameter), centered at the same η as the jet but $\pm\pi/2$ away in ϕ .

For the inclusive jet analysis, the average transverse momentum density per unit area deposited inside the two cones, \hat{p} , is computed and the correction $dp_T = \hat{p}A_{\text{jet}}$ is applied to the jet p_T . A_{jet} is the jet area and is given by the anti- k_T algorithm using the ghost particle method [39].

In the dijet analysis, the 4-momentum is calculated for the collection of particles in each off-axis cone, summed and then rotated by $\pm\pi/2$ back to the position of the jet.

After rotation, the off-axis cone 4-momenta are averaged, scaled to the area of the jet A_{jet} , and subtracted from the initial jet 4-momentum. The underlying event correction is calculated and applied on a jet-by-jet basis for both the dijet and the inclusive jet analyses.

This technique recognizes that the STAR detector has excellent four-fold symmetry in azimuth, but the efficiency is not as uniform in pseudorapidity. For example, there is a small gap in the EMC coverage between the BEMC and EEMC. Requiring the off-axis cones to be centered at the same η as the jet and sum over similar areas ensures the η dependence of the underlying event and other background contributions are sampled correctly, and facilitates the jet-by-jet correction. It is important to note that, in addition to accounting for the UE, this procedure also corrects for pileup effects arising, for example, from beam-beam and beam-gas collisions other than the pp collision of interest.

C. Dijet and inclusive jet event selection

Jets are selected for further analysis if the jet axis lies within $|\eta| < 0.9$ and the $p_T > 6$ GeV/ c . To minimize jet energy corrections near the detector acceptance limits, an additional z_{vertex} -dependent η cut ensures each jet thrust axis projects well within the BEMC. The remaining cuts are tuned specifically for the inclusive jet or dijet analysis and are detailed in the following sections.

1. Inclusive jet cuts

The jets are divided into three mutually exclusive groups depending on the highest jet patch trigger a specific jet can satisfy: JP0, JP1, or JP2. For example, a jet that deposited enough energy in the EMC to satisfy the JP1 trigger requirement, but fired only the JP0 trigger because of the JP1 prescale, is nonetheless categorized as JP1 during the analysis. In addition, each jet is required to point toward a jet patch that could trigger the event, including the constraints from prescales. The minimum reconstructed jet p_T values for the three trigger categories of 6.0, 8.2 and 15.3 GeV/ c , respectively, are set at p_T bin boundaries that are somewhat higher than the corresponding JP hardware trigger thresholds to reduce reconstruction bias near the trigger thresholds.

The summed transverse momenta of the charged tracks within a jet is required to be greater than 0.5 GeV/ c , and the fraction of jet energy detected in the EMCs, $R_{\text{EM}} = E_{\text{EM}}/(E_{\text{EM}} + E_{\text{track}})$, is required to be less than 0.94. These constraints suppress noncollision backgrounds such as cosmic events and beam backgrounds, which do not point back to the event vertex, and reduce the probability that the wrong vertex is assigned to the jet. The track momentum resolution degrades for $p_T > 30$ GeV/ c , so jets with such tracks are rejected.

Approximately 5% of the events in the inclusive jet analysis contain two jets, both of which satisfy all the cuts. In these cases, both jets are considered. Fewer than 0.05%

of events have three or more jets that satisfy all the cuts. For these cases, only the two jets with the highest p_T are considered.

2. Dijet cuts

Only events with two or more jets are considered for the dijet sample. From these events, the jets with the highest p_T are selected as the candidate dijet pair. At least one jet of the pair is required to point to a jet patch that satisfies the JP0, JP1 or JP2 trigger and to pass an associated threshold of 6.0, 8.0 or 15.0 GeV/ c , respectively. Both jets must have $R_{\text{EM}} < 0.95$. The latter constraint can be less stringent than used for inclusive jets because dijet events are less susceptible to backgrounds. The events are separated into three mutually exclusive groups (JP0, JP1, and JP2) using the same algorithm as for inclusive jets.

A dijet opening-angle cut, $\Delta\phi > 120^\circ$, is designed to remove the cases where one member of the dijet pair is the result of a hard gluon emission. An additional dijet opening-angle cut, $|\Delta\eta| < 1.6$, removes the kinematic region where both jets fall near the detector acceptance limits. A p_T -matching condition is applied that requires the ratio of the leading and away-side jet transverse momenta, $p_T^{\text{leading}}/p_T^{\text{away}} < (6 - 0.08p_T^{\text{max}})$, where p_T^{max} is the transverse momentum of the highest p_T track in either jet. This empirical cut was tuned on simulation and motivated by the need to remove fake jets that are composed nearly entirely of a single, poorly reconstructed TPC track. Finally, an asymmetric p_T cut requires one of the jets to have a $p_T > 8$ GeV/ c and the other $p_T > 6$ GeV/ c . The latter condition is motivated by theoretical considerations [43].

Identified dijets are sorted into four topological bins (A-D) based on the pseudorapidities of the individual jets in the dijet pair. Three pseudorapidity regions are defined as follows: forward spanning $0.3 < \eta < 0.9$, central spanning $-0.3 < \eta < 0.3$, and backward spanning $-0.9 < \eta < -0.3$. These three regions permit the construction of four unique topological bins, described in Table I. The dijets in bins A and B reflect the most asymmetric collisions in terms of partonic x_1 and x_2 and, therefore, sample the highest and lowest x values. The dijets in bins C and D originate from more symmetric partonic collisions, and largely access intermediate x values. Bins A and C sample collisions with $|\cos\theta^*|$ near zero, while bins B and D sample regions of

TABLE I. The four dijet topology bins A-D. In all cases, the dijet pair is also required to satisfy $\Delta\phi > 120^\circ$ and $|\Delta\eta| < 1.6$.

Bin	η_3 and η_4 Regions	Physics description
A	$0.3 < \eta_{3,4} < 0.9; \eta_3 \cdot \eta_4 > 0$	Forward-Forward
B	$ \eta_{3,4} < 0.3; 0.3 < \eta_{4,3} < 0.9$	Forward-Central
C	$ \eta_{3,4} < 0.3$	Central-Central
D	$0.3 < \eta_{3,4} < 0.9; \eta_3 \cdot \eta_4 < 0$	Forward-Backward

larger $|\cos \theta^*|$. The factor $\cos \theta^*$, where θ^* is the scattering angle in the partonic center-of-mass frame, enters directly into the calculation of the partonic asymmetry, \hat{a}_{LL} . For the present case, \hat{a}_{LL} is larger when $|\cos \theta^*|$ is smaller.

IV. EMBEDDED SIMULATION

A Monte Carlo simulation is used to determine corrections to the measured jet quantities and estimate contributions to the total systematic uncertainty. Simulated pp events generated by PYTHIA [44] are passed through a detailed GEANT3 [45] simulation of the STAR detector utilizing a geometry setup matching the 2012 detector configuration. The simulated detector responses are then embedded into zero-bias events, which were recorded without any trigger requirement at random times during the running period. In this way, the simulated events contain the same pile-up and beam backgrounds as the real data. After embedding, the simulated EMC tower ADCs are analyzed by the trigger simulator in order to identify those events that satisfy one or more of the jet patch triggers. If so, the embedded events are then passed through the full reconstruction and analysis routines that are used for the data. The intermediate parton and particle records from PYTHIA are saved for all generated events, including those that fail the trigger simulation, to facilitate the study of potential bias effects.

A. PYTHIA tune

QCD events were generated using PYTHIA version 6.4.28 [44] and the Perugia 2012 tune [46]. This combination overestimates the inclusive π^\pm yields by up to 30% for $p_T < 3$ GeV/c, when compared to the previously published STAR measurements at $\sqrt{s} = 200$ GeV [47,48]. To compensate, a single parameter in the Perugia 2012 PYTHIA tune, PARP(90), was reduced from 0.24 to 0.213. PARP(90) controls the energy dependence of the low- p_T cut-off for the UE generation process. After this change, the simulated inclusive π^\pm yields at $p_T < 3$ GeV/c match the experimentally measured cross sections within 10%. See [49] for a detailed discussion of the tuning process, including comparisons of the STAR experimental π^\pm cross sections to several tune options. See [50] for a detailed comparison of jet properties between default Perugia 2012 and our tuned version.

The full pp simulation sample consisted of tuned Pythia + Geant simulated events embedded into zero-bias events that were recorded without any required trigger condition throughout the running period. Jets were then reconstructed from the simulated detector responses using the same anti- k_T algorithm with $R = 0.5$ as was used to reconstruct jets in the data. The simulation provides an excellent description of many jet-related quantities, as shown in the next subsection. However, it slightly overestimates the rate of UE production seen in the data.

Systematic uncertainties to account for this mismatch are discussed in Sec. V.

B. Comparisons between data and simulation

Extensive comparisons of dijet and inclusive jet observables in the data and embedded simulation samples have been performed to ensure the simulation successfully reproduces the data. For the subset of these comparisons shown in Figs. 2–9, the UE subtraction has been applied in the same way to the detector jets in data and simulation. However, only raw, detector-level quantities are plotted, uncorrected for acceptance, efficiency, or resolution effects. When the statistical uncertainties are not visible, they are smaller than the data points.

1. Comparison of jet and dijet observables

Figure 2 shows the jet yields vs p_T in the data and embedding for the three trigger categories. There is an excellent match between data and embedding for all three categories.

Distributions of the charged hadrons within the jets are shown for data and simulation as functions of the hadron

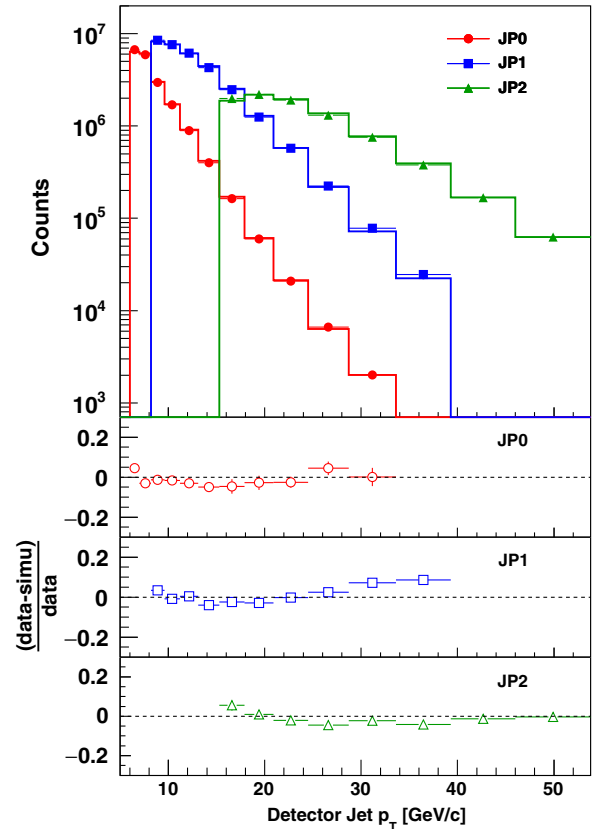


FIG. 2. The upper panel shows the jet yields vs detector jet p_T in data and simulation for each of the three trigger categories. The points show the data, and the histograms show the simulation. The lower three panels show the relative differences between data and simulation.

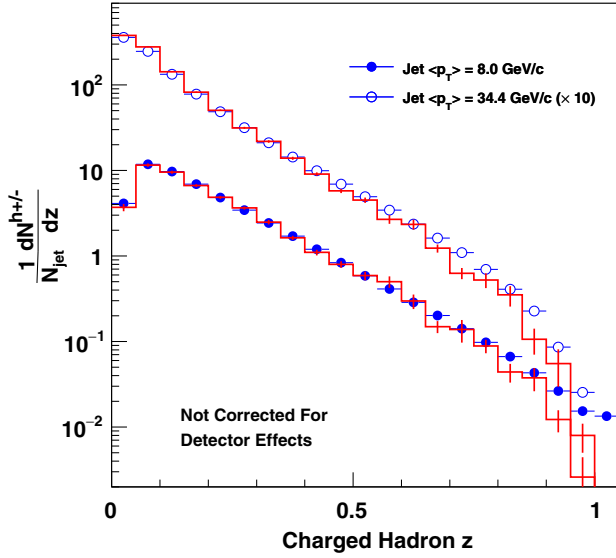


FIG. 3. Distributions of the charged hadrons within the jets as a function of the hadron longitudinal momentum fraction, z , for two typical detector jet p_T bins. The blue points show the data, and the red histograms show the simulation.

longitudinal momentum fraction, $z = p_{\text{hadron}}/p_{\text{jet}}$, and momentum transverse to the jet thrust axis, j_T , in Figs. 3 and 4. The distributions are shown for two representative detector jet p_T bins, 7.0–8.2 GeV/ c and 28.7–33.6 GeV/ c , which correspond to corrected mean jet p_T values of 8.0 and 34.4 GeV/ c (see Sec. V C).

An alternative view of the fragmentation and hadronization process is shown in Fig. 5, which illustrates the R_{EM} distributions for the same two jet p_T bins. The upper panel shows detector jets with $\langle p_T \rangle = 8.0$ GeV/ c . Only JP0-triggered jets contribute to this low- p_T bin and the reconstructed jet p_T is relatively close to the JP0 threshold, $E_T = 5.4$ GeV. This favors jets with a large electromagnetic fraction, since only the energy deposited in the EMCs is considered by the trigger. The jets with small R_{EM} values that nonetheless satisfied the trigger contain charged hadrons that deposited an unusually large fraction of their energy in the EMCs. This picture is reversed in the lower panel, which shows detector jets with $\langle p_T \rangle = 34.4$ GeV/ c . Typically, the jets in this momentum region require a large fraction of their energy to be carried by charged hadrons to be categorized as JP0 or JP1, instead of JP2. The exceptions that have large R_{EM} fractions typically were near the ϕ -boundary between nonoverlapping jet patches and shared their electromagnetic energy between them. The data and embedding distributions in Figs. 3, 4, and 5 match quite well, indicating that the simulations provide a very good description of the jet substructure.

Figure 6 shows the comparison of data and simulation for the dijet yield as a function of invariant mass, M_{inv} . The top panel in Fig. 7 shows the opening angle $\Delta\phi$ and the bottom the $\Delta\eta$ of the dijet pair. No significant differences

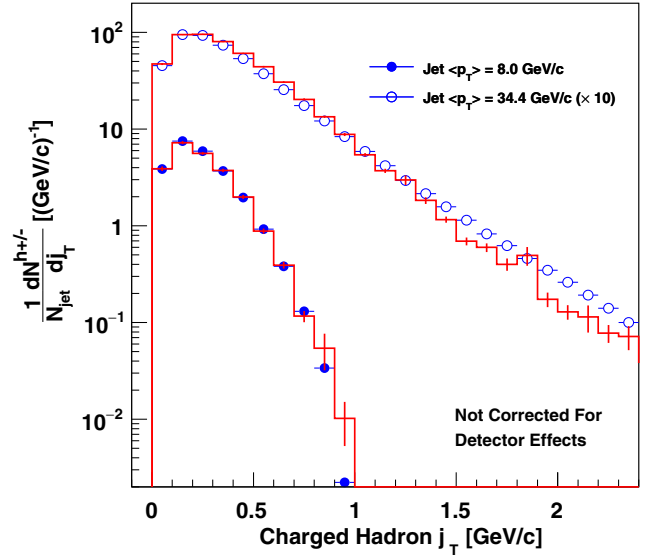


FIG. 4. Distributions of the charged hadrons within the jets as a function of the hadron momentum transverse to the thrust axis, j_T , for two typical detector jet p_T bins. The blue points show the data, and the red histograms show the simulation.

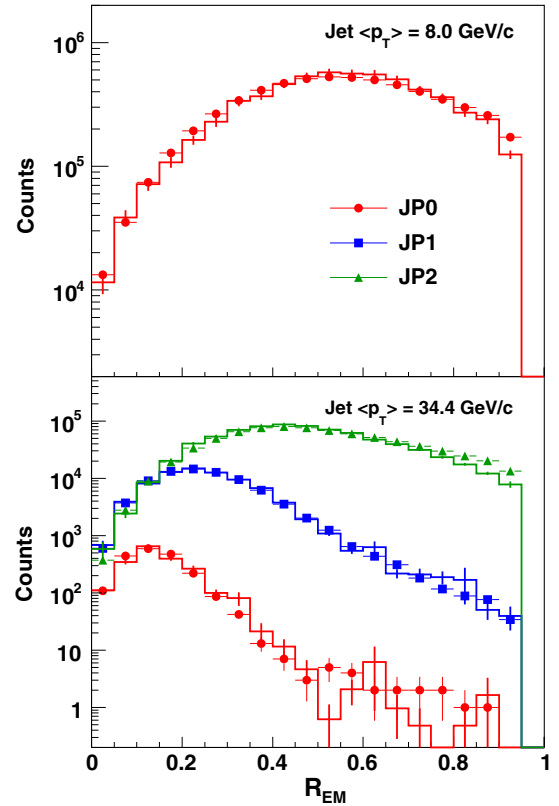


FIG. 5. The upper panel shows the electromagnetic fraction distribution, R_{EM} , for jets in a low- p_T bin. The bias in favor of large R_{EM} , driven by the proximity to the JP0 threshold, is clear. The lower panel shows the R_{EM} distributions in a higher p_T bin for each of the three jet categories. For this case, JP0 and JP1 jets have a bias in favor of small R_{EM} , as discussed in the text. The points show the data, and the histograms show the simulation.

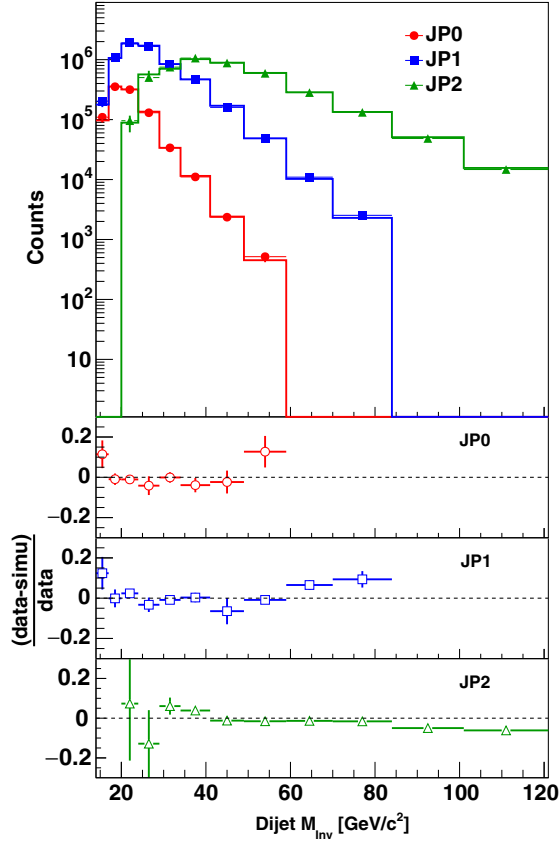


FIG. 6. Dijet yield vs invariant mass as measured at the detector level. In the top panel the data and simulations for the JP0, JP1 and JP2 trigger samples are represented by the points and histograms, respectively. The differences between data and simulation, normalized to the data yields, are shown for each of the trigger samples in the three bottom panels.

between the trigger samples were observed, therefore the independent trigger samples are combined, correctly accounting for run-time prescale in the simulation, for the $\Delta\phi$ and $\Delta\eta$ distributions. As with the inclusive yields, the agreement is excellent for the dijet observables.

2. Underlying event comparisons

Figure 8 shows the distributions of charged hadrons within the off-axis cones in data and simulation as a function of hadron p_T . The simulation provides a qualitative description of the observed UE hadrons. But quantitatively it overestimates the UE production in the region $p_T \lesssim 1.3$ GeV/c, as illustrated in the inset. The distributions of EMC tower E_T values in the off-axis cones (not shown) also reveal an excess yield in the simulation at low E_T .

The mean underlying event correction to the jet transverse momentum, dp_T , is shown in the upper panel of Fig. 9 as a function of detector jet p_T . The discontinuities in the UE dp_T distribution at 8.2 and 15.3 GeV/c, where the JP1 and JP2 event categories first contribute, originate from

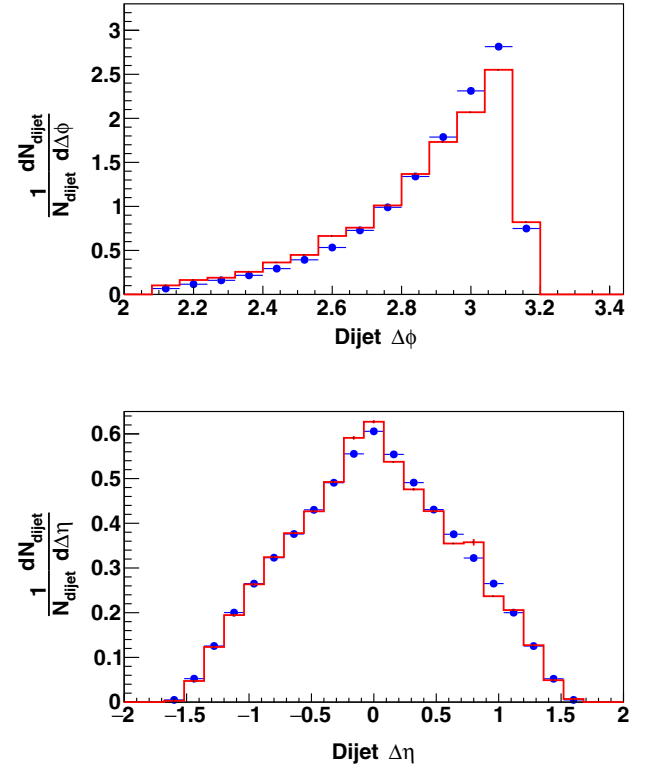


FIG. 7. Dijet opening angle $\Delta\phi$ (top) and $\Delta\eta$ (bottom) distributions. The blue points represent the data, and the red histograms the simulation.

a trigger bias effect. As discussed in Sec. II, the STAR jet trigger is based on the energy observed in the EMCs. The UE present in an event serves to lower the effective trigger thresholds for the jets of interest, and hence increase the

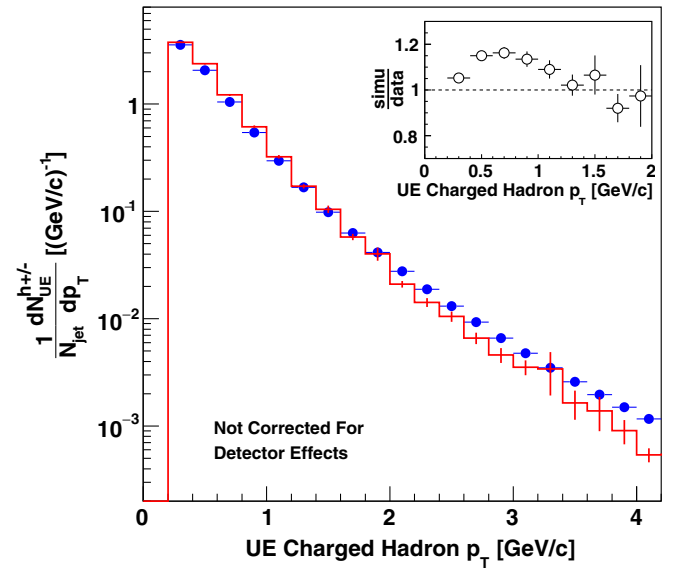


FIG. 8. Distributions of the charged hadrons within the off-axis cones as a function of hadron p_T . The blue points show the data, and the red histogram shows the simulation. The inset shows the ratio of simulation to data for $p_T < 2$ GeV/c.

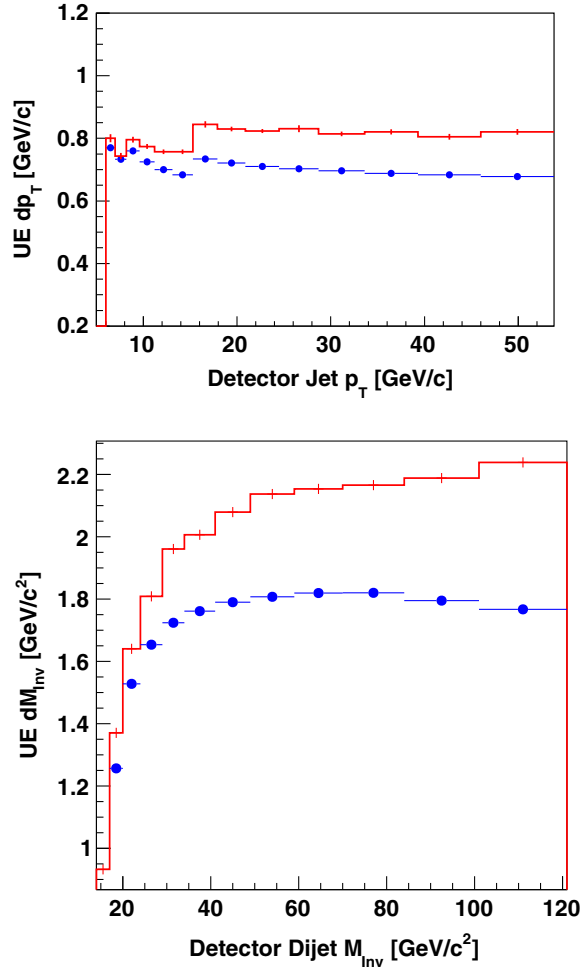


FIG. 9. The upper panel shows the mean underlying event correction to the jet transverse momentum, dp_T , as a function of detector jet p_T . The lower panel shows the mean underlying event correction to the dijet mass, dM_{inv} , as a function of M_{inv} . In both cases, the blue points show the data, and the red histogram shows the simulation.

trigger efficiency at a given jet p_T . This effect is maximal near the trigger turn-on points. The lower panel of Fig. 9 shows a similar comparison of the UE corrections to the dijet mass, dM_{inv} , in data and simulation. In this case the enhancements at the trigger thresholds are less pronounced because only one of the two jets in the dijet pair is required to fulfill the trigger threshold requirement.

Overall, the UE yield discrepancy between data and simulation seen in Figs. 8 and 9 causes the simulation to predict 10% to 20% larger dp_T and dM_{inv} than seen in the data. The implications of these differences are discussed in Sec. V.

C. Parton and particle jets

Up to this point, the discussion has focused on jet properties as they are reconstructed at the detector level, both in data and simulation. These properties are influenced

by finite detector acceptance, efficiency and resolution effects. The PYTHIA record for a simulated event affords the opportunity to relate these “detector jets” to more idealized jet objects. We do this in two ways. We reconstruct “particle jets” by running the anti- k_T algorithm over the complete set of stable particles produced in the event. The same off-axis cone UE correction procedure used for detector jets is applied to particle jets. We also reconstruct “parton jets” by running the anti- k_T algorithm on the hard-scattered partons from a given simulated PYTHIA event, including the initial-state and final-state radiation associated with the process, but excluding those partons from beam remnants and multiple parton interactions. In both cases, the jet finding algorithm and the input parameters to the algorithm are the same as used when reconstructing detector jets.

Detector jets reconstructed from the embedded simulation detector responses can be matched to companion parton or particle jets. In this analysis, a parton or particle jet is considered to match a detector jet if the distance between the jet thrust axes in $\eta - \phi$ space is $\sqrt{\Delta\eta^2 + \Delta\phi^2} < 0.5$. If more than one parton or particle jet matches a given detector jet, we choose the closest one in $\eta - \phi$ space. We then use the properties of the matched parton or particle jet when estimating corrections for the detector jets. The probability that a detector jet with $6.0 < p_T < 8.2$ GeV/c has a matching particle jet is 98%. For $p_T > 8.2$ GeV/c, over 99% of detector jets have a matching particle jet. The probability that a detector jet with $6.0 < p_T < 7.0$ GeV/c has a matching parton jet is 85%. The probability increases rapidly with increasing detector jet p_T , reaching $> 99\%$ for detector jet $p_T > 9.6$ GeV/c. Dijets are considered matched if each jet in the pair satisfies the inclusive jet matching criterion. The dijet detector-parton matching fractions range from 95%–97% for $M_{inv} = 14$ –17 GeV/c² and quickly reach unity by $M_{inv} = 24$ GeV/c². The improved matching fractions for the dijets compared to the inclusive jets is predominately due to the requirement to reconstruct two nearly back-to-back jets. This significantly cuts down on the reconstruction of fake jets and jets whose axis is badly reconstructed due to underlying event or background contributions.

As a further test of the UE subtraction procedure, we examine the difference in PYTHIA between the transverse momenta of UE-corrected particle jets and matched parton jets, $\delta p_T = p_{T,\text{parton}} - p_{T,\text{particle}}$. At low p_T , where relatively little initial- and final-state radiation accompanies the hard scattering, we find $\langle \delta p_T \rangle \approx 0.1$ GeV/c. This is a much smaller difference than was seen for low- p_T jets in our previous $\sqrt{s} = 200$ GeV analysis, where no UE correction was implemented [7]. At high p_T , where substantial gluon radiation often accompanies a hard scattering, the off-axis cones capture a small amount of initial- and final-state radiation, in addition to the UE, so the UE-corrected particle jet transverse momenta underestimate their matched parton jets by 2–3%.

V. LONGITUDINAL DOUBLE-SPIN ASYMMETRIES

The longitudinal double-spin asymmetry A_{LL} is defined as the difference of cross sections when the two beams have the same and opposite helicities divided by their sum:

$$A_{LL} = \frac{\sigma^{++} - \sigma^{+-}}{\sigma^{++} + \sigma^{+-}}. \quad (1)$$

In this analysis, A_{LL} is calculated as:

$$A_{LL} = \frac{\sum_{\text{runs}} P_Y P_B (N^{++} - r N^{+-})}{\sum_{\text{runs}} P_Y^2 P_B^2 (N^{++} + r N^{+-})}, \quad (2)$$

where $N^{++}(N^{+-})$ is the number of jets or dijets observed in a given run with the same (opposite) helicity beams, P_Y and P_B are the beam polarizations for the run, and the relative luminosity, $r = \mathcal{L}^{++}/\mathcal{L}^{+-}$, is the ratio of the luminosities for same and opposite helicity beams during the run. The beam polarizations and relative luminosities were treated as constant over the duration of a run. This was motivated by the fact that runs typically lasted 10–40 minutes, a short time period compared to changes in these beam properties.

A. Beam polarization

The CNI polarization measurements were performed at the beginning of each fill, at several hour increments during the fill, and at the end of each fill. The RHIC polarimetry group uses the results to determine the initial beam polarization at the beginning of the fill, P_0 , and the polarization decay rate, dP/dt [51]. For each run, the polarization is taken to be the interpolated value at the midpoint of the run. Following the guidance from the RHIC polarimetry group [51], the systematic uncertainty on the product of the two beam polarizations $P_Y P_B$ is 6.6% for the data used here. This is a common overall scale uncertainty for the final inclusive jet and dijet A_{LL} results.

B. Relative luminosity

The relative luminosity for each run is calculated using scalars that counted the number of VPD coincidences and VPD east and west singles bunch-by-bunch. The observed event counts for each bunch are corrected for accidental and multiple coincidences [52]. The corrected VPD coincidence yields, summed over all bunches in the run with the same spin combination ($++$, $+-$, $-+$, $--$), are then used to calculate the relative luminosity r for that run. The values of the relative luminosity vary fill-by-fill from 0.9 to 1.1, depending on the sequence of beam helicities used. Only very small variations are observed within fills.

To estimate the systematic uncertainty in the relative luminosity calculation, the ratios obtained from the corrected VPD coincidence yields are compared run-by-run to similar ratios calculated using the corrected VPD east

singles or west singles, and to the ratios calculated using the corrected number of ZDC coincidences, east singles, or west singles. A wide range of additional comparisons are made by considering alternative combinations of spin states, such as those appropriate to measure a parity-violating longitudinal single-spin asymmetry with the blue or yellow beam. Following this study, a systematic uncertainty of 1.3×10^{-4} is associated with r .

C. Scale corrections and systematic errors

A_{LL} varies slowly and approximately linearly over the full kinematic range of the current measurements. This makes it practical to implement a bin-by-bin unfolding technique to correct the inclusive jet p_T and dijet M_{inv} for detector resolution and efficiency effects. The matching conditions discussed in Sec. IV C are implemented in the simulation and the average partonic level p_T or M_{inv} is determined for each detector bin. The calculated asymmetry for that bin is then plotted at the average partonic p_T or M_{inv} value. This scale is chosen to facilitate a more direct comparison to the NLO pQCD theoretical predictions, which do not include effects from hadronization or underlying event contributions. The small, higher-order distortions from resolution and efficiency that remain are compensated as part of the trigger and reconstruction bias correction described below.

This type of correction requires an evaluation of the accuracy of the TPC track p_T and EMC E_T calibrations and efficiencies (labeled Hadron resp. and EM resp., respectively, in Tables II and III). The effect of the systematic overestimate of the underlying event in the simulation on the jet p_T and dijet M_{inv} , as well as the uncertainty in the PYTHIA tune, must also be quantified. Tables II and III present the estimated corrections for the inclusive jet transverse momentum and dijet mass scales and their systematic uncertainties. The following sub-subsections discuss them in more detail.

1. Detector response uncertainties

The shift in scale from the detector to the parton level depends on the accuracy of the TPC tracking efficiency implemented in the simulation. Studies of simulated pp collisions at $\sqrt{s} = 200$ GeV suggested a 4% uncertainty on the accuracy of the tracking efficiency [53]. A more conservative estimate of the uncertainty, 5%, is used here to reflect the reduction of tracking efficiency and increase in uncertainty that occurs at the higher luminosities in 510 GeV pp collisions.

The effect of the tracking efficiency uncertainty on the scale correction is calculated by first randomly rejecting 5% of all reconstructed TPC tracks in the embedded simulation sample, and then rerunning the jet finder. The differences between the jet p_T and dijet M_{inv} are taken as the systematic contributions due to tracking efficiency uncertainty.

TABLE II. The corrections and systematic uncertainties assigning parton jet p_T values to the detector-level inclusive jet p_T bins. The uncertainty quoted for $\delta p_T = \langle p_{T,\text{parton}} - p_{T,\text{detector}} \rangle$ is the contribution from the simulation statistics. All values are in GeV/ c .

Detector jet								Parton jet
Bin	p_T range	$\langle p_T \rangle$	δp_T	Hadron resp.	EM resp.	UE syst.	Tune syst.	p_T
I1	6.0–7.0	6.48	0.54 ± 0.07	0.10	0.15	0.03	0.18	7.02 ± 0.26
I2	7.0–8.2	7.56	0.41 ± 0.07	0.16	0.16	0.01	0.18	7.97 ± 0.30
I3	8.2–9.6	8.86	1.04 ± 0.06	0.19	0.20	0.04	0.22	9.90 ± 0.36
I4	9.6–11.2	10.35	1.21 ± 0.05	0.21	0.22	0.05	0.25	11.56 ± 0.40
I5	11.2–13.1	12.07	1.30 ± 0.06	0.28	0.24	0.06	0.27	13.37 ± 0.47
I6	13.1–15.3	14.09	1.52 ± 0.05	0.34	0.26	0.07	0.24	15.61 ± 0.50
I7	15.3–17.9	16.52	2.47 ± 0.08	0.35	0.36	0.11	0.30	18.99 ± 0.60
I8	17.9–20.9	19.28	2.88 ± 0.05	0.39	0.42	0.11	0.23	22.17 ± 0.63
I9	20.9–24.5	22.52	3.14 ± 0.05	0.47	0.47	0.11	0.30	25.66 ± 0.74
I10	24.5–28.7	26.36	3.30 ± 0.06	0.60	0.52	0.13	0.21	29.65 ± 0.83
I11	28.7–33.6	30.81	3.56 ± 0.07	0.70	0.57	0.12	0.26	34.38 ± 0.95
I12	33.6–39.3	36.00	3.72 ± 0.08	0.82	0.64	0.13	0.22	39.7 ± 1.1
I13	39.3–46.0	42.06	4.26 ± 0.09	0.96	0.74	0.12	0.19	46.3 ± 1.2
I14	46.0–53.8	49.14	4.67 ± 0.11	1.11	0.85	0.14	0.49	53.8 ± 1.5

There is an uncertainty associated with how well our GEANT simulation models the energy deposited in the EMCs by hadrons [54] that are either not detected by the TPC or are detected but deposit some of their energy outside of the tower pointed to by the track. This

contribution to the systematic error varies from 1.5% of the jet p_T at low p_T to 2% at high p_T .

The EMC gains are established using a combination of minimum-ionizing particles and identified electrons. The calibration uncertainty for 2012 is estimated to be 3.8%.

TABLE III. The corrections and systematic uncertainties assigning parton dijet M_{inv} to the detector-level dijet M_{inv} bins. The four topology groups are described in detail in Table I. The uncertainty quoted for $\delta M_{\text{inv}} = \langle M_{\text{inv,parton}} - M_{\text{inv,detector}} \rangle$ is the contribution from the simulation statistics. All values are in GeV/ c^2 .

Detector dijet								Parton dijet
Bin	M_{inv} range	$\langle M_{\text{inv}} \rangle$	δM_{inv}	Hadron resp.	EM resp.	UE syst.	Tune syst.	M_{inv}
Topology A: Forward-Forward Dijets								
A1	14–17	15.88	3.16 ± 0.28	0.41	0.30	0.16	0.58	19.04 ± 0.82
A2	17–20	18.48	3.14 ± 0.22	0.58	0.34	0.14	0.63	21.62 ± 0.96
A3	20–24	21.93	4.45 ± 0.17	0.59	0.39	0.12	0.78	26.38 ± 1.08
A4	24–29	26.34	5.96 ± 0.23	0.73	0.49	0.18	0.70	32.30 ± 1.16
A5	29–34	31.35	7.07 ± 0.24	0.85	0.57	0.24	0.52	38.42 ± 1.20
A6	34–41	37.19	7.99 ± 0.23	1.17	0.71	0.15	0.50	45.18 ± 1.48
A7	41–49	44.55	8.87 ± 0.26	1.17	0.82	0.27	0.48	53.42 ± 1.55
A8	49–59	53.23	10.29 ± 0.27	1.43	0.94	0.28	0.42	63.52 ± 1.80
A9	59–70	63.58	11.97 ± 0.34	1.81	1.09	0.39	0.40	75.55 ± 2.21
A10	70–84	75.49	13.63 ± 0.42	1.90	1.26	0.28	0.48	89.12 ± 2.38
Topology B: Forward-Central Dijets								
B1	14–17	16.01	2.79 ± 0.28	0.44	0.31	0.09	0.53	18.80 ± 0.81
B2	17–20	18.52	3.28 ± 0.16	0.54	0.35	0.10	0.66	21.80 ± 0.94
B3	20–24	21.94	4.43 ± 0.12	0.73	0.40	0.11	0.69	26.37 ± 1.09
B4	24–29	26.34	5.90 ± 0.14	0.71	0.49	0.16	0.61	32.24 ± 1.07
B5	29–34	31.36	7.06 ± 0.17	0.97	0.60	0.26	0.55	38.42 ± 1.31
B6	34–41	37.22	8.61 ± 0.16	1.04	0.72	0.27	0.53	45.83 ± 1.41
B7	41–49	44.58	9.56 ± 0.16	1.30	0.85	0.27	0.57	54.14 ± 1.69
B8	49–59	53.30	10.87 ± 0.18	1.44	0.98	0.33	0.42	64.17 ± 1.83
B9	59–70	63.67	12.39 ± 0.24	1.72	1.12	0.30	0.39	76.06 ± 2.13
B10	70–84	75.67	14.14 ± 0.27	2.02	1.30	0.38	0.39	89.81 ± 2.48
B11	84–101	90.68	17.24 ± 0.34	2.36	1.53	0.46	0.33	107.92 ± 2.89

(Table continued)

TABLE III. (Continued)

Detector dijet								Parton dijet
Bin	M_{inv} range	$\langle M_{\text{inv}} \rangle$	δM_{inv}	Hadron resp.	EM resp.	UE syst.	Tune syst.	M_{inv}
Topology C: Central-Central Dijets								
C1	14–17	15.89	3.92 ± 0.34	0.33	0.32	0.16	0.56	19.81 ± 0.81
C2	17–20	18.49	3.52 ± 0.24	0.50	0.34	0.05	0.91	22.01 ± 1.12
C3	20–24	21.93	4.23 ± 0.24	0.73	0.41	0.08	0.63	26.16 ± 1.08
C4	24–29	26.34	6.36 ± 0.26	0.64	0.50	0.09	0.81	32.70 ± 1.19
C5	29–34	31.36	7.35 ± 0.29	1.05	0.61	0.21	0.43	38.71 ± 1.34
C6	34–41	37.22	8.79 ± 0.28	0.90	0.73	0.35	0.56	46.01 ± 1.36
C7	41–49	44.57	9.32 ± 0.32	1.35	0.86	0.40	0.57	53.89 ± 1.78
C8	49–59	53.31	11.44 ± 0.35	1.25	0.99	0.36	0.48	64.75 ± 1.74
C9	59–70	63.65	13.50 ± 0.39	1.84	1.14	0.37	0.45	77.15 ± 2.27
C10	70–84	75.70	15.44 ± 0.49	2.06	1.32	0.33	0.58	91.14 ± 2.58
Topology D: Forward-Backward Dijets								
D1	14–17	16.34	4.20 ± 0.60	0.90	0.32	−0.23	0.56	20.54 ± 2.14
D2	17–20	18.68	3.41 ± 0.34	0.57	0.35	0.01	0.91	22.09 ± 0.95
D3	20–24	21.97	4.34 ± 0.23	0.59	0.40	0.10	0.63	26.31 ± 0.98
D4	24–29	26.37	5.35 ± 0.24	0.72	0.47	0.12	0.81	31.72 ± 1.22
D5	29–34	31.36	7.12 ± 0.32	0.84	0.57	0.18	0.43	38.48 ± 1.31
D6	34–41	37.25	7.96 ± 0.29	1.17	0.70	0.22	0.56	45.21 ± 1.55
D7	41–49	44.65	9.50 ± 0.33	1.25	0.84	0.28	0.57	54.15 ± 1.69
D8	49–59	53.39	10.91 ± 0.30	1.49	0.97	0.35	0.48	64.30 ± 1.92
D9	59–70	63.72	12.94 ± 0.36	1.69	1.12	0.36	0.45	76.66 ± 2.15
D10	70–84	75.76	13.81 ± 0.44	2.14	1.29	0.34	0.58	89.57 ± 2.62
D11	84–101	90.82	16.04 ± 0.55	2.42	1.52	0.39	0.41	106.86 ± 2.97

We apply this to the observed electromagnetic energy fractions R_{EM} , leading to scale uncertainties that range from 2.2% at low p_T to 1.7% at high p_T .

In addition to the three effects discussed above, there are smaller (<1%) contributions from the uncertainty in the EMC efficiency simulation and the TPC momentum calibration.

2. Underlying event correction

The full 10% to 20% difference between data and simulation for the underlying event dp_T and dM_{inv} corrections is taken as the systematic uncertainty. The uncertainty is calculated on a bin-by-bin basis for the jet and dijet distributions.

3. PYTHIA tune variation

A change in the parameters of the Perugia 2012 PYTHIA tune may, in turn, cause a shift in the average partonic jet p_T and dijet M_{inv} determined for the scale correction. The nature and size of the shift is studied by implementing several relevant variants [46] of the Perugia 2012 tune in PYTHIA and recalculating the corrections.

The alternative tunes selected include the choice of $\alpha_s(\frac{1}{2}p_\perp)$ and $\alpha_s(2p_\perp)$ for higher (tune 371) and lower (tune 372) initial- and final-state radiation respectively, the modification to less color re-connections (tune 374), the

increase in either longitudinal (376) or transverse (377) fragmentations, a switch to MSTW 2008 LO PDFs rather than CTEQ6L1 LO PDFs (378), and a set of Innsbruck hadronization parameters (383). For additional details regarding the alternative PYTHIA tunes, see [50].

The corrections for alternative tune pairs (371, 372) and (376, 377), which relate to initial + final state radiation and fragmentation respectively, bracket those for the default tune. Therefore, half of the absolute difference of the pair is taken as its contribution to the tune systematic uncertainty. Together with the difference in scale shift from the remaining tunes, they are added in quadrature to construct the total PYTHIA tune systematic error.

D. Asymmetry corrections and systematic errors

A broad range of systematic contributions to the measured A_{LL} values are considered. For low- p_T jets the dominant contributions arise from UE and relative luminosity uncertainties, while trigger and reconstruction bias dominates at high p_T . The same trend is observed as function of M_{inv} for the dijet sample. Several other effects are evaluated and found to be negligible compared to the statistical and leading systematic uncertainties. Tables IV and V present the estimated corrections and systematic uncertainties for the inclusive jet and dijet A_{LL} values, respectively. The following sub-subsections describe these estimates.

TABLE IV. The corrections and systematic uncertainties in A_{LL} for inclusive jet production. In addition to the uncertainties enumerated here, there are two that are common to all the points, a shift uncertainty of ± 0.00022 associated with the relative luminosity measurement and a scale uncertainty of $\pm 6.6\%$ associated with the beam polarization.

Bin	Jet p_T (GeV/ c)	UE syst.	Trigger and reconstruction bias			Total syst.
			Correction	PDF uncert.	Stat+vertex syst.	
I1	7.02	0.00029	-0.00012	0.00013	0.00003	0.00013
I2	7.97	0.00024	-0.00007	0.00037	0.00032	0.00049
I3	9.90	0.00022	-0.00021	0.00007	0.00008	0.00011
I4	11.56	0.00018	-0.00014	0.00007	0.00004	0.00008
I5	13.37	0.00016	-0.00024	0.00008	0.00007	0.00011
I6	15.61	0.00013	-0.00027	0.00009	0.00013	0.00016
I7	18.99	0.00012	-0.00033	0.00011	0.00009	0.00014
I8	22.17	0.00011	-0.00026	0.00019	0.00013	0.00023
I9	25.66	0.00009	-0.00039	0.00013	0.00012	0.00018
I10	29.65	0.00008	-0.00034	0.00020	0.00015	0.00025
I11	34.38	0.00007	-0.00033	0.00025	0.00028	0.00038
I12	39.7	0.00006	-0.00004	0.00019	0.00028	0.00034
I13	46.3	0.00006	0.00042	0.00052	0.00045	0.00069
I14	53.8	0.00005	0.00011	0.00056	0.00059	0.00081

1. Underlying event contribution

Underlying event contributions both lower the effective JP trigger thresholds and increase the apparent energy of the reconstructed jets. Thus, if the UE has a spin

dependence, it can distort the measured dijet and inclusive jet A_{LL} values. To examine this possibility, we measured the longitudinal double-spin asymmetry of the underlying event contributions, $A_{LL}^{dp_T}$ and $A_{LL}^{dM_{inv}}$. We define

TABLE V. The corrections and systematic uncertainties in A_{LL} for dijet production. In addition to the uncertainties enumerated here, there are two that are common to all the points, a shift uncertainty of ± 0.00022 associated with the relative luminosity measurement and a scale uncertainty of $\pm 6.6\%$ associated with the beam polarization. The four topology groups are described in detail in Table I.

	Dijet M_{inv}		Trigger and reconstruction bias			
Bin	(GeV/ c^2)	UE syst.	Model correction	Model error	Stat. error	Total error
Topology A: Forward-Forward Dijets						
A1	19.04	−0.00013	0.00057	0.00021	0.00002	0.00022
A2	21.62	0.00054	0.00071	0.00023	0.00004	0.00024
A3	26.38	0.00058	0.00119	0.00037	0.00003	0.00037
A4	32.30	0.00051	0.00109	0.00037	0.00001	0.00037
A5	38.42	0.00046	0.00184	0.00044	0.00001	0.00044
A6	45.18	0.00041	0.00143	0.00060	0.00001	0.00060
A7	53.42	0.00038	0.00246	0.00089	0.00001	0.00089
A8	63.52	0.00030	0.00077	0.00102	0.00004	0.00102
A9	75.55	0.00030	0.00256	0.00200	0.00005	0.00200
A10	89.12	0.00022	0.00658	0.00479	0.00002	0.00479
Topology B: Forward-Central Dijets						
B1	18.80	−0.00034	0.00058	0.00020	0.00002	0.00020
B2	21.80	0.00059	0.00085	0.00028	0.00001	0.00028
B3	26.37	0.00034	0.00113	0.00033	0.00002	0.00033
B4	32.24	0.00037	0.00101	0.00042	0.00001	0.00042
B5	38.42	0.00028	0.00172	0.00045	0.00003	0.00046
B6	45.83	0.00028	0.00115	0.00065	0.00001	0.00065
B7	54.14	0.00021	0.00112	0.00078	0.00001	0.00078
B8	64.17	0.00021	0.00245	0.00111	0.00003	0.00111
B9	76.06	0.00018	0.00278	0.00137	0.00001	0.00137
B10	89.81	0.00014	0.00519	0.00199	0.00001	0.00199
B11	107.92	0.00014	0.00732	0.00270	0.00003	0.00270

(Table continued)

TABLE V. (Continued)

	Dijet M_{inv}		Trigger and reconstruction bias			
Bin	(GeV/ c^2)	UE syst.	Model correction	Model error	Stat. error	Total error
Topology C: Central-Central Dijets						
C1	19.81	−0.00015	0.00015	0.00019	0.00004	0.00019
C2	22.01	0.00059	0.00027	0.00063	0.00008	0.00064
C3	26.16	0.00070	0.00135	0.00041	0.00002	0.00041
C4	32.70	0.00075	−0.00090	0.00057	0.00007	0.00057
C5	38.71	0.00078	0.00193	0.00069	0.00002	0.00069
C6	46.01	0.00048	0.00131	0.00058	0.00001	0.00058
C7	53.89	0.00048	0.00263	0.00117	0.00003	0.00117
C8	64.75	0.00035	0.00148	0.00143	0.00003	0.00143
C9	77.15	0.00035	0.00282	0.00185	0.00004	0.00185
C10	91.14	0.00035	−0.00050	0.00732	0.00003	0.00732
Topology D: Forward-Backward Dijets						
D1	20.54	−0.00129	0.00067	0.00022	0.00003	0.00022
D2	22.09	−0.00005	0.00065	0.00024	0.00003	0.00024
D3	26.31	0.00068	0.00086	0.00029	0.00004	0.00029
D4	31.72	0.00047	0.00132	0.00032	0.00002	0.00032
D5	38.48	0.00050	0.00113	0.00041	0.00001	0.00042
D6	45.21	0.00038	0.00151	0.00053	0.00007	0.00053
D7	54.15	0.00039	0.00171	0.00077	0.00002	0.00077
D8	64.30	0.00028	0.00296	0.00112	0.00001	0.00112
D9	76.66	0.00028	0.00482	0.00238	0.00002	0.00238
D10	89.57	0.00028	0.00273	0.00142	0.00001	0.00142
D11	106.86	0.00019	0.00178	0.00282	0.00003	0.00282

$$A_{LL}^{dp_T} = \frac{1}{P_Y P_B} \frac{\langle dp_T \rangle^{++} - \langle dp_T \rangle^{+-}}{\langle dp_T \rangle^{++} + \langle dp_T \rangle^{+-}}, \quad (3)$$

where $\langle dp_T \rangle^{++}$ and $\langle dp_T \rangle^{+-}$ are the average underlying event corrections for same and opposite beam helicity combinations. A similar definition is used for $A_{LL}^{dM_{\text{inv}}}$. Figure 10 shows the observed $A_{LL}^{dp_T}$ as a function of detector jet p_T . The results in Fig. 10 are not corrected for finite detector acceptance, efficiency, or resolution.

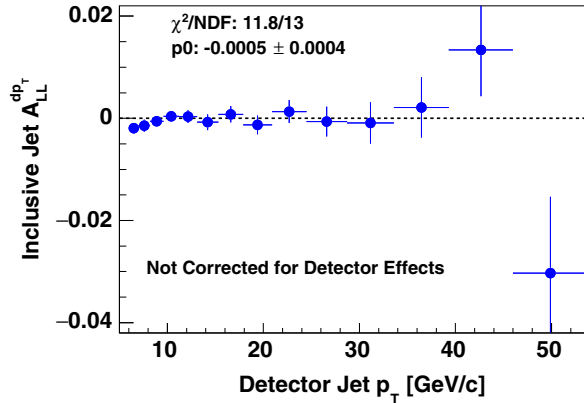


FIG. 10. Observed $A_{LL}^{dp_T}$ vs detector jet p_T . Note that no corrections have been made for detector acceptance, efficiency, or resolution.

However, these effects, which are independent of the beam spin combination, are expected to contribute similarly to the numerator and denominator in Eq. (3). A constant fit finds $A_{LL}^{dp_T} = -0.0005 \pm 0.0004$, with $\chi^2 = 11.8$ for 13 degrees of freedom. A similar estimate was performed for each topology bin in the dijet analysis. The constant fit to the measured UE $A_{LL}^{dM_{\text{inv}}}$ for topology bin A finds $A_{LL}^{dM_{\text{inv}}} = -0.0014 \pm 0.0017$, for bin B finds $A_{LL}^{dM_{\text{inv}}} = 0.0012 \pm 0.0011$, for bin C finds $A_{LL}^{dM_{\text{inv}}} = -0.0035 \pm 0.0021$, and for bin D finds $A_{LL}^{dM_{\text{inv}}} = 0.0028 \pm 0.0015$, with associated χ^2 per degrees of freedom values ranging from 0.5–1.2. Within the present statistics, $A_{LL}^{dp_T}$ and $A_{LL}^{dM_{\text{inv}}}$ are consistent with zero and independent of jet p_T and dijet M_{inv} .

To estimate the possible systematic contribution that the UE can make to the measured inclusive jet (dijet) A_{LL} values, we calculate the change in the cross section that would occur if the effective boundaries of our jet p_T (M_{inv}) bins shift in a spin-dependent manner by an amount equal to the observed dp_T (dM_{inv}) values multiplied by either the average UE asymmetry or the error, whichever is larger. For the inclusive jets the corresponding systematic uncertainties vary from 2.9×10^{-4} for the lowest p_T bin to 0.5×10^{-4} for the highest p_T bin. The dijet analysis follows a similar trend with errors of order $\approx 1 \times 10^{-3}$ in the lower M_{inv} bins that reduce to the level of $\approx 2 \times 10^{-4}$ in the

highest M_{inv} bins. Since underlying event effects are expected to be independent of the hard scale and we use the overall average from the full data set to set the limit in the inclusive jet analysis, we treat these uncertainties as fully correlated. For the dijets, the errors are treated as fully correlated within a single topological bin.

2. Relative luminosity uncertainty

The contribution to the total systematic uncertainty due to relative luminosity can be approximated as $\Delta A_{LL} = \frac{1}{2P_Y P_B} \times \frac{\Delta r}{r}$. Taking $P_Y = 54\%$, $P_B = 55\%$, and $\Delta r/r = 1.3 \times 10^{-4}$, as calculated in Sec. VB, this systematic uncertainty is estimated as 2.2×10^{-4} . It represents the possible offset of the $A_{LL} = 0$ axis, and is common to all the measured inclusive and dijet asymmetries.

3. Trigger bias and reconstruction uncertainty

The jet matching calculations in Sec. VC closely align our jet measurements with those expected for unbiased parton jets, but the match is not perfect. This is illustrated in Fig. 11, which shows the sampled gluon x distributions, weighted by the partonic asymmetry \hat{a}_{LL} to indicate the region that is sensitive to $\Delta g(x)$. At high jet p_T , the agreement is very good. In contrast, at low jet p_T , there is a small but clear shift in x between the unbiased distribution and the distribution that is sampled by the jets that are successfully triggered and reconstructed. This difference arises from several trigger and reconstruction bias effects. For example, quark and gluon jets fragment differently, which can lead to different trigger efficiencies for gluon-gluon, quark-gluon, and quark-quark scattering

processes. Detector and trigger resolutions might also distort the measured asymmetries. We utilize our embedding simulation to calculate a correction, and an associated uncertainty, to our measured A_{LL} values to account for these trigger and reconstruction bias effects. At high collision rates, there is a small probability that low- p_T jets will be assigned to the wrong vertex and, hence, misreconstructed. We utilize the same embedding simulation to estimate the probability that the wrong vertex is found.

The average luminosity during 2012 corresponds to ≈ 0.6 inelastic collisions per bunch crossing. At this rate, there is a small probability that the highest quality vertex selected by the vertex finder was not the actual jet vertex. We estimate this by comparing the reconstructed z_{vertex} in the simulation sample to the known position where the PYTHIA event was embedded. For the two lowest- p_T bins in the inclusive jet measurement, the wrong vertex is selected 15% of the time. This causes the jet kinematics, most especially the pseudorapidity, to be misreconstructed. We assign a systematic uncertainty to A_{LL} for these two bins, calculated by assuming events with the wrong vertex introduce a dilution of the true asymmetry. The probability to assign a jet to the wrong vertex is $\leq 4\%$ for the remaining inclusive jet p_T bins, which makes this uncertainty negligible in all other cases. The probability to assign a dijet to the wrong vertex is less than 1% for all invariant mass bins except for the forward-forward topology where the very lowest mass bins have a 5%–7% probability for a mismatched vertex. The quality of the vertex reconstruction is directly related to the number of tracks in the event and leads to the improved vertex matching found in the dijet sample.

To estimate the remaining trigger and reconstruction biases, we compare the dijet and inclusive jet A_{LL} values found by the simulation at the detector jet and parton jet levels. To calculate A_{LL} in the simulation, we weight each event by the product of the leading-order $2 \rightarrow 2$ partonic asymmetry \hat{a}_{LL} and the ratio of polarized and unpolarized parton distribution functions of the two scattered partons,

$$w = \hat{a}_{LL} \frac{\Delta f_1(x_1, Q^2) \Delta f_2(x_2, Q^2)}{f_1(x_1, Q^2) f_2(x_2, Q^2)}. \quad (4)$$

In principle, this requires knowledge of the polarized PDFs that we want to determine. Lacking that, we calculate A_{LL} using each of the 100 available equally probable replica sets that have been provided to span the range of polarized PDF uncertainties in NNPDFpol1.1 [14]. The average difference between the A_{LL} found for all parton jets or dijets, including those from events that failed the trigger or detector jet reconstruction, and that for reconstructed detector jets or dijets is taken to be the correction for residual trigger and reconstruction bias effects. The root-mean-square of the parton vs detector A_{LL} differences obtained with the 100 replica sets is assigned as a

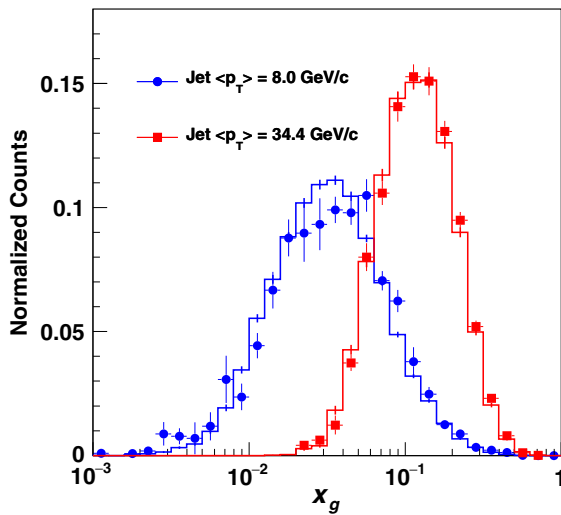


FIG. 11. The \hat{a}_{LL} -weighted gluon x distributions for two inclusive jet p_T bins. The histograms represent all parton jets, independent of whether the jets satisfy the trigger and reconstruction requirements, while the points show the triggered detector jets. Comparisons without the \hat{a}_{LL} weight are qualitatively similar.

systematic uncertainty associated with our lack of knowledge of the true polarized PDFs. This systematic is treated as fully correlated for all the A_{LL} results. We also assign a point-to-point systematic uncertainty to account for the finite statistics of the simulation.

Tables IV and V show that the trigger and reconstruction bias corrections are most significant at intermediate jet p_T and dijet M_{inv} . For the lowest jet p_T and dijet M_{inv} values, which sample gluon x values below the region that has been constrained by data in previous global analyses, the PDF uncertainties are larger than the calculated corrections. At the highest jet p_T and dijet M_{inv} values, where the calculated bias is small, the statistical uncertainties dominate. Nonetheless, the calculated corrections and their uncertainties are always small compared to the statistical uncertainties in the measured A_{LL} results.

4. Other potential effects

Residual transverse components of the beam polarization can distort the A_{LL} measurement when coupled to the transverse double-spin asymmetry A_Σ [6]. The residual transverse components of the beam polarization were monitored by the ZDC throughout the running period. Comparing the transverse asymmetries measured by the ZDC during transverse and longitudinal running periods, we find the transverse fractions of the total beam polarizations are approximately 5% and 3% for the blue and yellow beams, respectively. A_Σ has not yet been measured in $\sqrt{s} = 510$ GeV collisions, but it has been measured to be less than 0.008 in the relevant x range at $\sqrt{s} = 200$ GeV [6]. If we take this as an upper limit, the contribution due to the residual transverse double-spin asymmetry is less than 3×10^{-5} , which is negligible compared to the other uncertainties.

Noncollision backgrounds can distort the A_{LL} measurement if they satisfy our jet cuts. To estimate the non-collision background fraction, jets are reconstructed from the abort gaps in the same way as from the normal bunch crossings. Abort gaps are sequential bunch crossings where one of the beams has intentionally been left unfilled. Typically nine of the 120 bunch crossings in each beam were left unfilled during the 2012 running period. After cuts, the jet yield is reduced by four orders of magnitude relative to the yield from the normal bunch crossings, even though measures of the background rates in the zero-bias events are similar for both normal and abort gap crossings. We conclude that noncollision backgrounds have a negligible impact on the A_{LL} results.

At $\sqrt{s} = 510$ GeV, the parity-violating longitudinal single-spin asymmetry, A_L , is expected to be negligible compared to our current statistical precision. Therefore, we examine the blue and yellow beam single-spin asymmetries A_L^B and A_L^Y as a consistency check of the relative luminosity calculations and an indicator of bunch-dependent collider instrumental effects. As expected, the

observed asymmetries are consistent with zero and subsequently no corresponding systematic uncertainty is assigned.

E. Correlations

Most of the dijet events contain at least one jet that satisfies the inclusive jet cuts. This leads to significant statistical correlations between the dijet and inclusive jet results, as large as 0.21, when the dijet M_{inv} is close to twice the inclusive jet p_T . As noted in Sec. III C 1, a small fraction ($\simeq 5\%$) of the events in the inclusive jet analysis contain two jets, both of which satisfy the inclusive jet cuts. This produces statistical correlations between the inclusive jet asymmetry measurements that range from 0.01 for low- p_T pairs of inclusive jet bins to 0.04 for high- p_T pairs. In contrast, there are no statistical correlations between the dijet asymmetry measurements.

There are also correlated point-to-point systematic effects, as discussed in the previous subsection, though they are typically smaller than the statistical correlations. We treat the inclusive jet UE systematic uncertainty estimates in Table IV as fully correlated because they are all derived from the same fit to the $A_{LL}^{dp_T}$ measurements shown in Fig. 10. Similarly, we treat the dijet UE systematic uncertainty estimates in Table V as fully correlated for each topology group because each dijet UE uncertainty is derived from the fit to the $A_{LL}^{dM_{inv}}$ measurements for that specific topology group. The PDF systematic uncertainties in Tables IV and V are highly correlated for measurements that sample nearby x values. The correlation is weaker for measurements that sample more distant x values. To be conservative, we nonetheless treat all the PDF systematic uncertainties as fully correlated. In all cases, the total point-to-point systematic correlations are estimated to be < 0.06 . The full correlation matrix for the inclusive jet and dijet A_{LL} measurements, including both the statistical and point-to-point systematic uncertainties, is given in the Appendix.

There are two systematic uncertainties, relative luminosity and beam polarization, that are common to all of the measurements and are not included in the correlation matrix presented in the Appendix. Note that the $\pm 6.6\%$ polarization scale uncertainty is common not just to the measurements here, but to all double-spin asymmetry measurements that are derived from 2012 RHIC data at $\sqrt{s} = 510$ GeV, including those in [25,26]. Furthermore, a substantial fraction of the polarization scale uncertainty arises from uncertainty in the molecular hydrogen fraction in the hydrogen gas-jet target, and this uncertainty is correlated across several years of RHIC operation. See [51] for details.

VI. RESULTS AND IMPACT

The inclusive jet and dijet A_{LL} are presented as functions of the fully corrected parton-level jet p_T and dijet M_{inv} in

TABLE VI. A_{LL} as a function of parton jet p_T (in GeV/c) for inclusive jets with $|\eta| < 0.9$ in $\sqrt{s} = 510$ GeV pp collisions. There is an additional $\pm 6.6\%$ scale uncertainty from the beam polarization that is common to all the measurements. The underlying event and relative luminosity systematics are fully correlated for all the points.

Bin	Jet p_T	$A_{LL} \pm \text{stat.} \pm \text{syst.}$	UE/RL syst.
I1	7.02 ± 0.26	$0.0000 \pm 0.0013 \pm 0.0001$	0.00036
I2	7.97 ± 0.30	$-0.0022 \pm 0.0014 \pm 0.0005$	0.00033
I3	9.90 ± 0.36	$0.0016 \pm 0.0010 \pm 0.0001$	0.00031
I4	11.56 ± 0.40	$0.0005 \pm 0.0011 \pm 0.0001$	0.00028
I5	13.37 ± 0.47	$0.0015 \pm 0.0013 \pm 0.0001$	0.00027
I6	15.61 ± 0.50	$0.0029 \pm 0.0016 \pm 0.0002$	0.00026
I7	18.99 ± 0.60	$0.0016 \pm 0.0016 \pm 0.0001$	0.00025
I8	22.17 ± 0.63	$0.0044 \pm 0.0018 \pm 0.0002$	0.00025
I9	25.66 ± 0.74	$0.0050 \pm 0.0021 \pm 0.0002$	0.00024
I10	29.65 ± 0.83	$0.0036 \pm 0.0027 \pm 0.0003$	0.00023
I11	34.38 ± 0.95	$0.0169 \pm 0.0037 \pm 0.0004$	0.00023
I12	39.7 ± 1.1	$-0.0049 \pm 0.0054 \pm 0.0003$	0.00023
I13	46.3 ± 1.2	$0.0122 \pm 0.0084 \pm 0.0007$	0.00023
I14	53.8 ± 1.5	$0.0018 \pm 0.0137 \pm 0.0008$	0.00023

Tables VI and VII. Figure 12 shows the inclusive jet asymmetries and systematic uncertainties compared to the theoretical predictions from the DSSV14 [13] and

NNPDFpol1.1 [14] global analyses. The red lines are the statistical errors while the size of the red boxes represent the uncorrelated systematic uncertainties on A_{LL} (vertical) and parton jet p_T (horizontal). The correlated errors, which include the underlying event systematic uncertainty on A_{LL} combined in quadrature with the relative luminosity systematic uncertainty, are plotted as a gray band on the horizontal axis.

The theory curves were generated by utilizing the polarized PDFs in the NLO jet production code of Mukherjee and Vogelsang [20]. Both theory curves, which include gluon polarization data from RHIC only for energies up to $\sqrt{s} = 200$ GeV, show very good agreement with the measured asymmetries. The solid blue region represents the nominal one-sigma error band for NNPDFpol1.1. This uncertainty corresponds to the root-mean-square of the distribution of 100 equally probable replica predictions represented by the green lines. This figure clearly demonstrates the ability of these data to constrain the existing polarized PDF uncertainties, which are driven by uncertainties in the gluon helicity distribution.

In the region of kinematic overlap, the $\sqrt{s} = 510$ GeV inclusive jet asymmetries are statistically consistent with the previous measurements at $\sqrt{s} = 200$ GeV [7]. This is demonstrated in Fig. 13, which compares A_{LL} as a function

TABLE VII. A_{LL} as a function of parton dijet M_{inv} (in GeV/c²) in $\sqrt{s} = 510$ GeV pp collisions. There is an additional $\pm 6.6\%$ scale uncertainty from the beam polarization that is common to all the measurements. The underlying event and relative luminosity systematics are fully correlated for each topology group. The four topology groups are described in detail in Table I.

Bin	Dijet M_{inv}	$A_{LL} \pm \text{stat.} \pm \text{syst.}$	UE/RL syst.
Topology A: Forward-Forward Dijets			
A1	19.04 ± 0.82	$-0.0128 \pm 0.0066 \pm 0.0002$	0.00025
A2	21.62 ± 0.96	$0.0090 \pm 0.0052 \pm 0.0002$	0.00058
A3	26.38 ± 1.08	$0.0079 \pm 0.0050 \pm 0.0004$	0.00062
A4	32.30 ± 1.16	$-0.0012 \pm 0.0052 \pm 0.0004$	0.00056
A5	38.42 ± 1.20	$0.0101 \pm 0.0061 \pm 0.0004$	0.00051
A6	45.18 ± 1.48	$-0.0013 \pm 0.0064 \pm 0.0006$	0.00046
A7	53.42 ± 1.55	$0.0048 \pm 0.0081 \pm 0.0009$	0.00044
A8	63.52 ± 1.80	$0.0052 \pm 0.0108 \pm 0.0010$	0.00037
A9	75.55 ± 2.21	$0.0363 \pm 0.0167 \pm 0.0020$	0.00037
A10	89.12 ± 2.38	$-0.0218 \pm 0.0264 \pm 0.0048$	0.00031
Topology B: Forward-Central Dijets			
B1	18.80 ± 0.81	$-0.0023 \pm 0.0053 \pm 0.0002$	0.00040
B2	21.80 ± 0.94	$0.0041 \pm 0.0036 \pm 0.0003$	0.00063
B3	26.37 ± 1.09	$0.0016 \pm 0.0033 \pm 0.0003$	0.00041
B4	32.24 ± 1.07	$0.0029 \pm 0.0034 \pm 0.0004$	0.00043
B5	38.42 ± 1.31	$-0.0063 \pm 0.0040 \pm 0.0005$	0.00035
B6	45.83 ± 1.41	$0.0020 \pm 0.0041 \pm 0.0007$	0.00036
B7	54.14 ± 1.69	$0.0128 \pm 0.0050 \pm 0.0008$	0.00030
B8	64.17 ± 1.83	$-0.0022 \pm 0.0065 \pm 0.0011$	0.00031
B9	76.06 ± 2.13	$-0.0010 \pm 0.0096 \pm 0.0014$	0.00028
B10	89.81 ± 2.48	$-0.0160 \pm 0.0143 \pm 0.0020$	0.00026
B11	107.92 ± 2.89	$-0.0205 \pm 0.0242 \pm 0.0027$	0.00026

(Table continued)

TABLE VII. (Continued)

Bin	Dijet M_{inv}	$A_{LL} \pm \text{stat.} \pm \text{syst.}$	UE/RL syst.
Topology C: Central-Central Dijets			
C1	19.81 ± 0.81	$0.0058 \pm 0.0085 \pm 0.0002$	0.00026
C2	22.01 ± 1.12	$-0.0006 \pm 0.0066 \pm 0.0006$	0.00063
C3	26.16 ± 1.08	$-0.0043 \pm 0.0062 \pm 0.0004$	0.00074
C4	32.70 ± 1.19	$0.0049 \pm 0.0065 \pm 0.0006$	0.00078
C5	38.71 ± 1.34	$0.0046 \pm 0.0077 \pm 0.0007$	0.00081
C6	46.01 ± 1.36	$0.0155 \pm 0.0079 \pm 0.0006$	0.00052
C7	53.89 ± 1.78	$-0.0045 \pm 0.0098 \pm 0.0012$	0.00053
C8	64.75 ± 1.74	$0.0104 \pm 0.0127 \pm 0.0014$	0.00041
C9	77.15 ± 2.27	$0.0346 \pm 0.0192 \pm 0.0019$	0.00041
C10	91.14 ± 2.58	$0.0593 \pm 0.0294 \pm 0.0073$	0.00041
Topology D: Forward-Backward Dijets			
D1	20.54 ± 2.14	$0.0054 \pm 0.0161 \pm 0.0002$	0.00131
D2	22.09 ± 0.95	$0.0042 \pm 0.0051 \pm 0.0002$	0.00022
D3	26.31 ± 0.98	$0.0051 \pm 0.0050 \pm 0.0003$	0.00072
D4	31.72 ± 1.22	$-0.0031 \pm 0.0059 \pm 0.0003$	0.00052
D5	38.48 ± 1.31	$-0.0018 \pm 0.0060 \pm 0.0004$	0.00054
D6	45.21 ± 1.55	$-0.0040 \pm 0.0070 \pm 0.0005$	0.00044
D7	54.15 ± 1.69	$0.0034 \pm 0.0087 \pm 0.0008$	0.00044
D8	64.30 ± 1.92	$0.0050 \pm 0.0123 \pm 0.0011$	0.00036
D9	76.66 ± 2.15	$0.0058 \pm 0.0178 \pm 0.0024$	0.00036
D10	89.57 ± 2.62	$0.0291 \pm 0.0296 \pm 0.0014$	0.00036
D11	106.86 ± 2.97	$-0.0055 \pm 0.0461 \pm 0.0028$	0.00029

of $x_T = 2p_T/\sqrt{s}$ for the two energies. The extended kinematic reach of the 510 GeV asymmetries to lower x_T values is also seen in Fig. 13. The jet x_T is correlated

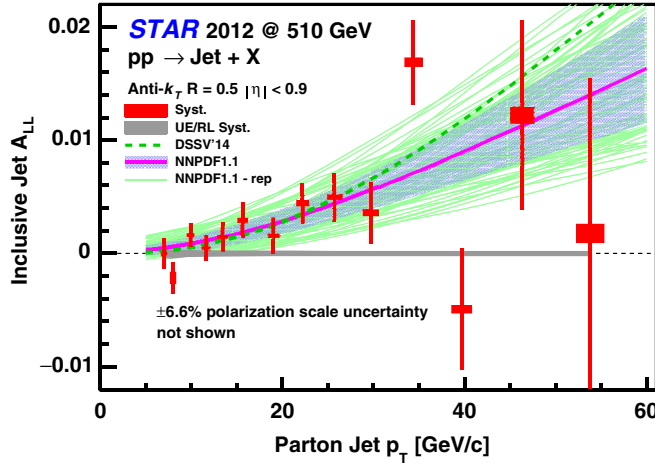


FIG. 12. A_{LL} as a function of parton jet p_T for inclusive jets with $|\eta| < 0.9$ in $\sqrt{s} = 510$ GeV pp collisions. The bars show statistical errors, while the size of the boxes show the point-to-point systematic uncertainties on A_{LL} (vertical) and p_T (horizontal). The gray band on the horizontal axis represents the combined relative luminosity and underlying event uncertainties, which are common to all the points. The results are compared to predictions from DSSV14 [13] and NNPDF1.1 [14], including the solid blue uncertainty band for the latter. The green curves are predictions from the 100 equally probable NNPDF1.1 replicas.

with the initial partonic longitudinal momentum fraction x , translating into a sensitivity to lower x partons as well. Figure 11 shows that the new inclusive jet results extend the sensitivity to gluon polarization down to $x \simeq 0.015$.

The broad x_g distributions in Fig. 11 show the wide range of x sampled by each inclusive jet p_T bin. In contrast, the

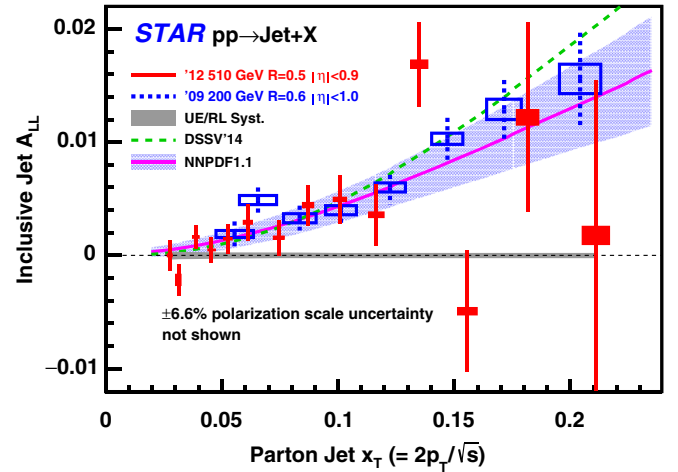


FIG. 13. A_{LL} as a function of x_T for inclusive jets in $\sqrt{s} = 510$ GeV pp collisions (red solid lines), compared to previous measurements of A_{LL} at $\sqrt{s} = 200$ GeV (blue dotted lines) [7]. The size of the boxes show the systematic uncertainties. Predictions from DSSV14 [13] and NNPDF1.1 [14], including the solid blue uncertainty band for the latter, are shown for $\sqrt{s} = 510$ GeV. Predictions for $\sqrt{s} = 200$ GeV are similar.

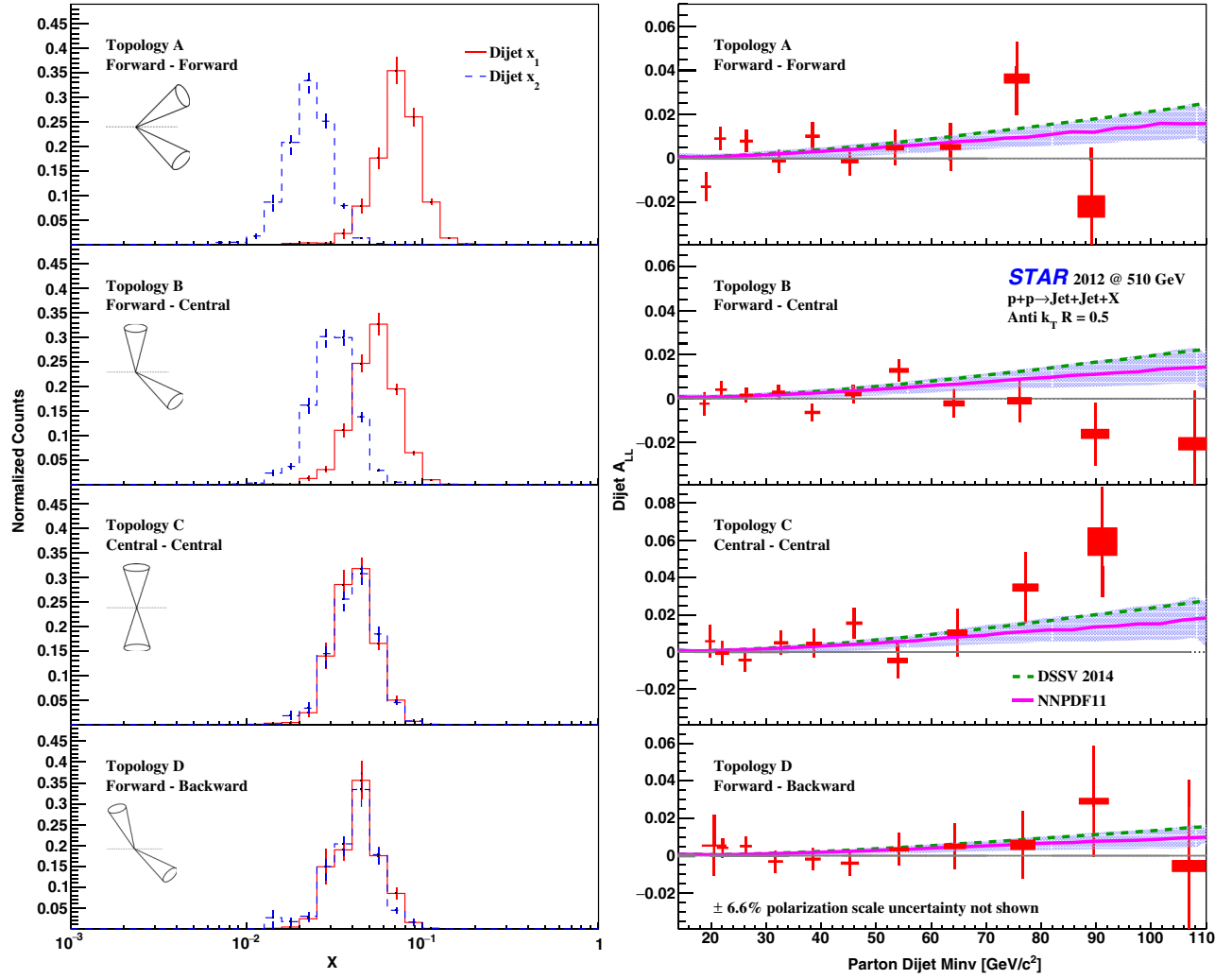


FIG. 14. Left: Leading order extractions from the embedding sample of the x_1 (red) and x_2 (blue) distributions in dijet events with $M_{\text{inv}} = 17\text{--}20 \text{ GeV}/c^2$ for topological bins A-D, which are defined in detail in Table I. The small figures illustrate the approximate orientations of the two jets relative to the beam line. Right: Dijet A_{LL} for the same topological bins in $\sqrt{s} = 510 \text{ GeV}$ pp collisions. The results are compared to theoretical predictions from DSSV14 and NNPDF11.

dijets permit full reconstruction of the initial x_1 and x_2 at leading order. The left-hand side panels in Fig. 14 show the leading order extractions, from the embedded simulation sample, of the x_1 and x_2 distributions for a single dijet bin $M_{\text{inv}} = 17\text{--}20 \text{ GeV}/c^2$. The $x_{1,2}$ values are calculated according to the leading order equations discussed in the introduction using the fully corrected jet p_T . The difference between x_1 and x_2 is largest for topological bin A (top) and decreases until they are identical in topological bins C and D. For all dijet bins, the widths of the x_1 and x_2 distributions are much narrower than those for the inclusive jet bins, providing a finer resolution on the x dependence of the extracted $\Delta g(x)$.

The right-hand side panels in Fig. 14 show the dijet A_{LL} as a function of the fully corrected parton-level M_{inv} for the same topological-bin ordering as the left-hand side. The statistical errors are shown by red bars, while the vertical

and horizontal width of the red boxes represent the uncorrelated systematic errors on the asymmetries and mass scale, respectively. The correlated errors, which include the underlying event systematic uncertainty on A_{LL} combined in quadrature with the relative luminosity systematic uncertainty, are plotted as a gray band on the horizontal axis. The dijet asymmetries are compared to the same NLO theoretical predictions as in the inclusive case, DSSV14 [13] and NNPDF11 [14]. The solid blue bands represent the PDF uncertainties for the NNPDF11 curves. Scale uncertainties were also calculated for NNPDF11 and found to be negligible in comparison to the PDF uncertainties. The predicted asymmetries are larger for the central-central topology than for the forward-backward combination, even though the x ranges sampled are very similar, because the smaller $\Delta\eta$ between the jets maximizes $\hat{a}_{LL}(\cos(\theta^*))$. Generally the

data show good agreement with the theoretical predictions, although with reduced statistical precision compared to the inclusive channel. There are regions, for example at low (high) M_{inv} in bin A(B) where the data will impact future global analyses of the polarized parton distribution, demonstrating the complementarity of the dijet and inclusive jet observables.

VII. CONCLUSION

We have presented measurements of the longitudinal double-spin asymmetry A_{LL} for inclusive jet and dijet production at midrapidity in pp collisions at $\sqrt{s} = 510$ GeV, based on data that were recorded by the STAR Collaboration during the 2012 RHIC running period. The results are sensitive to the gluon polarization over the momentum fraction range from $x \approx 0.015$ to $x \approx 0.2$. The inclusive jet results will provide important new constraints on the magnitude of the gluon polarization and the dijet results will provide important new constraints on the shape of $\Delta g(x)$ when they are included in future global analyses of the polarized PDFs, especially in the region $x < 0.05$ that has been unconstrained by input data in previous global analyses.

ACKNOWLEDGMENTS

We thank the RHIC Operations Group and RCF at BNL, the NERSC Center at LBNL, and the Open Science Grid consortium for providing resources and support. This work was supported in part by the Office of Nuclear Physics within the U.S. DOE Office of Science, the U.S. National Science Foundation, the Ministry of Education and Science of the Russian Federation, National Natural Science Foundation of China, Chinese Academy of Science, the Ministry of Science and Technology of China and the Chinese Ministry of Education, the National Research Foundation of Korea, Czech Science Foundation and Ministry of Education, Youth and Sports of the Czech Republic, Hungarian National Research, Development and Innovation Office, New National Excellency Programme of the Hungarian Ministry of Human Capacities, Department of Atomic Energy and Department of Science and Technology of the Government of India, the National Science Centre of Poland, the Ministry of Science, Education and Sports of the Republic of Croatia, RosAtom of Russia and German Bundesministerium für Bildung, Wissenschaft, Forschung und Technologie (BMBF) and the Helmholtz Association.

APPENDIX: CORRELATION MATRIX

The inclusive jet and dijet A_{LL} results presented here have two systematic uncertainties that are common to all the data points. The relative luminosity uncertainty represents a common offset of the $A_{LL} = 0$ axis by $\pm 2.2 \times 10^{-4}$. An uncertainty of $\pm 6.6\%$ in the product of the beam polarizations represents an overall scale uncertainty. In addition, there are point-to-point statistical and systematic correlations, as discussed in Sec. V E. The correlation matrix that quantifies these additional point-to-point effects is given in Tables VIII–XXII. The entries that are not shown can be obtained by transposition.

TABLE VIII. The correlation matrix for the point-to-point uncertainties in the inclusive jet measurements. At low p_T , the dominant effects arise from correlated systematic uncertainties, whereas at high p_T , the dominant effects arise from the statistical correlations when two jets in the same event satisfy all the inclusive jet cuts. The relative luminosity and beam polarization uncertainties, which are common to all the data points, are not included.

Bin	I1	I2	I3	I4	I5	I6	I7	I8	I9	I10	I11	I12	I13	I14
I1	1	0.065	0.057	0.044	0.036	0.026	0.024	0.024	0.016	0.013	0.011	0.006	0.007	0.005
I2		1	0.056	0.045	0.039	0.030	0.031	0.036	0.023	0.023	0.020	0.010	0.016	0.011
I3			1	0.046	0.039	0.030	0.027	0.024	0.016	0.013	0.009	0.005	0.006	0.004
I4				1	0.035	0.028	0.025	0.022	0.014	0.011	0.008	0.005	0.005	0.003
I5					1	0.029	0.026	0.023	0.015	0.012	0.009	0.005	0.005	0.003
I6						1	0.025	0.023	0.016	0.012	0.009	0.005	0.005	0.003
I7							1	0.028	0.022	0.019	0.014	0.008	0.008	0.005
I8								1	0.029	0.027	0.022	0.014	0.012	0.008
I9									1	0.030	0.026	0.018	0.014	0.008
I10										1	0.035	0.028	0.022	0.013
I11											1	0.037	0.031	0.020
I12												1	0.041	0.030
I13													1	0.044
I14														1

TABLE IX. The correlation matrix for the point-to-point uncertainties coupling the inclusive jet measurements with the forward-forward dijet measurements (Topology A). The relative luminosity and beam polarization uncertainties, which are common to all the data points, are not included.

Bin	A1	A2	A3	A4	A5	A6	A7	A8	A9	A10
I1	0.020	0.011	0.009	0.007	0.007	0.009	0.010	0.009	0.011	0.017
I2	0.027	0.025	0.023	0.018	0.018	0.023	0.027	0.023	0.029	0.044
I3	0.066	0.054	0.029	0.013	0.006	0.006	0.007	0.006	0.008	0.012
I4	0.033	0.062	0.056	0.025	0.009	0.006	0.006	0.006	0.007	0.010
I5	0.006	0.053	0.064	0.053	0.020	0.010	0.007	0.006	0.007	0.011
I6	0.002	0.023	0.058	0.064	0.042	0.018	0.008	0.005	0.007	0.010
I7	0.002	0.005	0.047	0.072	0.078	0.059	0.024	0.009	0.008	0.012
I8	0.003	0.005	0.026	0.059	0.073	0.096	0.059	0.023	0.014	0.019
I9	0.002	0.003	0.008	0.034	0.052	0.081	0.103	0.052	0.018	0.012
I10	0.002	0.003	0.005	0.016	0.031	0.056	0.086	0.116	0.048	0.021
I11	0.002	0.003	0.005	0.007	0.015	0.031	0.057	0.093	0.124	0.047
I12	0.001	0.002	0.003	0.003	0.005	0.012	0.026	0.057	0.096	0.131
I13	0.002	0.003	0.005	0.004	0.005	0.008	0.014	0.029	0.063	0.116
I14	0.001	0.002	0.003	0.003	0.003	0.004	0.006	0.011	0.026	0.064

TABLE X. The correlation matrix for the point-to-point uncertainties coupling the inclusive jet measurements with the forward-central dijet measurements (Topology B). The relative luminosity and beam polarization uncertainties, which are common to all the data points, are not included.

Bin	B1	B2	B3	B4	B5	B6	B7	B8	B9	B10	B11
I1	0.028	0.020	0.013	0.012	0.011	0.015	0.015	0.016	0.013	0.013	0.010
I2	0.033	0.043	0.035	0.032	0.028	0.038	0.038	0.041	0.034	0.034	0.027
I3	0.086	0.085	0.051	0.024	0.011	0.011	0.010	0.011	0.009	0.009	0.007
I4	0.032	0.090	0.087	0.046	0.018	0.012	0.009	0.010	0.008	0.008	0.006
I5	0.005	0.063	0.094	0.089	0.037	0.019	0.011	0.011	0.009	0.009	0.007
I6	0.002	0.022	0.082	0.094	0.078	0.035	0.014	0.010	0.008	0.008	0.006
I7	0.003	0.006	0.055	0.101	0.109	0.103	0.043	0.019	0.010	0.010	0.008
I8	0.004	0.008	0.027	0.080	0.103	0.138	0.105	0.047	0.020	0.015	0.012
I9	0.002	0.005	0.008	0.043	0.071	0.114	0.147	0.101	0.033	0.012	0.007
I10	0.003	0.006	0.007	0.020	0.041	0.078	0.119	0.171	0.094	0.031	0.010
I11	0.003	0.005	0.007	0.010	0.020	0.043	0.077	0.131	0.185	0.089	0.023
I12	0.001	0.003	0.003	0.004	0.006	0.017	0.035	0.076	0.134	0.200	0.072
I13	0.002	0.005	0.006	0.008	0.007	0.012	0.019	0.040	0.081	0.156	0.208
I14	0.002	0.003	0.004	0.005	0.005	0.006	0.008	0.016	0.035	0.086	0.179

TABLE XI. The correlation matrix for the point-to-point uncertainties coupling the inclusive jet measurements with the central-central dijet measurements (Topology C). The relative luminosity and beam polarization uncertainties, which are common to all the data points, are not included.

Bin	C1	C2	C3	C4	C5	C6	C7	C8	C9	C10
I1	0.016	0.014	0.008	0.008	0.008	0.007	0.011	0.011	0.009	0.023
I2	0.021	0.034	0.020	0.022	0.022	0.018	0.029	0.027	0.023	0.059
I3	0.051	0.045	0.024	0.012	0.007	0.005	0.008	0.007	0.006	0.016
I4	0.026	0.052	0.044	0.022	0.009	0.005	0.007	0.007	0.006	0.014
I5	0.004	0.046	0.052	0.045	0.018	0.008	0.008	0.007	0.006	0.015
I6	0.001	0.021	0.047	0.055	0.038	0.015	0.008	0.006	0.005	0.013
I7	0.002	0.008	0.036	0.057	0.062	0.046	0.021	0.010	0.007	0.017
I8	0.002	0.010	0.020	0.048	0.060	0.077	0.051	0.023	0.012	0.025
I9	0.001	0.006	0.006	0.028	0.044	0.065	0.086	0.045	0.015	0.016
I10	0.002	0.007	0.005	0.015	0.027	0.046	0.073	0.096	0.041	0.025
I11	0.002	0.006	0.004	0.007	0.015	0.025	0.049	0.080	0.102	0.047
I12	0.001	0.003	0.002	0.003	0.005	0.010	0.024	0.051	0.083	0.112
I13	0.001	0.006	0.004	0.005	0.006	0.006	0.014	0.027	0.055	0.108
I14	0.001	0.004	0.003	0.004	0.004	0.003	0.006	0.012	0.024	0.064

TABLE XII. The correlation matrix for the point-to-point uncertainties coupling the inclusive jet measurements with the forward-backward dijet measurements (Topology D). The relative luminosity and beam polarization uncertainties, which are common to all the data points, are not included.

Bin	D1	D2	D3	D4	D5	D6	D7	D8	D9	D10	D11
I1	0.011	0.018	0.011	0.006	0.007	0.007	0.008	0.009	0.012	0.005	0.006
I2	0.011	0.029	0.026	0.017	0.017	0.019	0.022	0.022	0.032	0.012	0.015
I3	0.030	0.060	0.047	0.023	0.010	0.006	0.006	0.006	0.009	0.003	0.004
I4	0.004	0.042	0.061	0.043	0.019	0.009	0.006	0.005	0.008	0.003	0.004
I5	0.001	0.016	0.056	0.061	0.038	0.018	0.008	0.006	0.008	0.003	0.004
I6	0.001	0.004	0.034	0.057	0.057	0.037	0.014	0.006	0.007	0.003	0.003
I7	0.001	0.003	0.015	0.054	0.065	0.076	0.045	0.018	0.011	0.004	0.004
I8	0.001	0.005	0.008	0.034	0.056	0.078	0.085	0.047	0.023	0.006	0.007
I9	0.001	0.003	0.004	0.013	0.035	0.059	0.080	0.089	0.042	0.011	0.005
I10	0.001	0.003	0.004	0.005	0.018	0.036	0.060	0.091	0.096	0.036	0.010
I11	0.001	0.003	0.004	0.004	0.008	0.019	0.035	0.064	0.101	0.098	0.030
I12	0.000	0.002	0.002	0.002	0.003	0.006	0.015	0.032	0.064	0.109	0.094
I13	0.001	0.003	0.004	0.003	0.004	0.005	0.009	0.016	0.036	0.068	0.127
I14	0.001	0.002	0.002	0.002	0.003	0.003	0.004	0.006	0.016	0.033	0.076

TABLE XIII. The correlation matrix for the point-to-point uncertainties in the forward-forward dijet measurements (Topology A). The relative luminosity and beam polarization uncertainties, which are common to all the data points, are not included.

Bin	A1	A2	A3	A4	A5	A6	A7	A8	A9	A10
A1	1	0.003	0.004	0.004	0.004	0.004	0.004	0.003	0.004	0.006
A2		1	0.015	0.013	0.011	0.011	0.010	0.007	0.007	0.009
A3			1	0.016	0.014	0.014	0.013	0.010	0.011	0.014
A4				1	0.012	0.013	0.012	0.009	0.010	0.013
A5					1	0.011	0.011	0.009	0.010	0.013
A6						1	0.013	0.010	0.012	0.017
A7							1	0.012	0.014	0.020
A8								1	0.012	0.017
A9									1	0.021
A10										1

TABLE XIV. The correlation matrix for the point-to-point uncertainties coupling the forward-forward dijet measurements (Topology A) with the forward-central dijet measurements (Topology B). The relative luminosity and beam polarization uncertainties, which are common to all the data points, are not included.

Bin	B1	B2	B3	B4	B5	B6	B7	B8	B9	B10	B11
A1	0.001	0.002	0.003	0.004	0.004	0.005	0.005	0.005	0.004	0.004	0.004
A2	0.002	0.003	0.004	0.005	0.005	0.007	0.007	0.007	0.006	0.006	0.005
A3	0.003	0.006	0.007	0.009	0.008	0.011	0.011	0.012	0.010	0.010	0.008
A4	0.003	0.005	0.007	0.009	0.008	0.011	0.011	0.012	0.010	0.010	0.008
A5	0.003	0.005	0.007	0.009	0.008	0.011	0.011	0.012	0.010	0.010	0.008
A6	0.004	0.007	0.009	0.011	0.010	0.015	0.014	0.016	0.013	0.013	0.010
A7	0.004	0.008	0.011	0.013	0.012	0.017	0.017	0.018	0.015	0.015	0.012
A8	0.004	0.007	0.009	0.011	0.010	0.015	0.014	0.016	0.013	0.013	0.010
A9	0.004	0.009	0.012	0.014	0.013	0.019	0.018	0.020	0.017	0.016	0.013
A10	0.007	0.014	0.018	0.022	0.020	0.028	0.027	0.030	0.025	0.025	0.020

TABLE XV. The correlation matrix for the point-to-point uncertainties coupling the forward-forward dijet measurements (Topology A) with the central-central dijet measurements (Topology C). The relative luminosity and beam polarization uncertainties, which are common to all the data points, are not included.

Bin	C1	C2	C3	C4	C5	C6	C7	C8	C9	C10
A1	0.001	0.003	0.002	0.003	0.003	0.002	0.004	0.004	0.003	0.008
A2	0.001	0.004	0.003	0.004	0.004	0.003	0.005	0.005	0.004	0.011
A3	0.002	0.007	0.005	0.006	0.007	0.005	0.009	0.008	0.007	0.018
A4	0.002	0.007	0.005	0.006	0.006	0.005	0.008	0.008	0.007	0.017
A5	0.002	0.007	0.005	0.006	0.006	0.005	0.008	0.008	0.007	0.017
A6	0.002	0.009	0.006	0.008	0.008	0.007	0.011	0.010	0.009	0.023
A7	0.002	0.010	0.007	0.009	0.010	0.008	0.013	0.012	0.010	0.026
A8	0.002	0.009	0.006	0.008	0.008	0.007	0.011	0.011	0.009	0.023
A9	0.003	0.011	0.008	0.010	0.011	0.009	0.014	0.013	0.011	0.029
A10	0.004	0.017	0.012	0.015	0.016	0.013	0.021	0.020	0.017	0.043

TABLE XVI. The correlation matrix for the point-to-point uncertainties coupling the forward-forward dijet measurements (Topology A) with the forward-backward dijet measurements (Topology D). The relative luminosity and beam polarization uncertainties, which are common to all the data points, are not included.

Bin	D1	D2	D3	D4	D5	D6	D7	D8	D9	D10	D11
A1	0.000	0.001	0.002	0.002	0.002	0.002	0.003	0.003	0.004	0.002	0.002
A2	0.001	0.002	0.003	0.002	0.003	0.003	0.004	0.004	0.006	0.002	0.003
A3	0.001	0.003	0.004	0.004	0.005	0.006	0.006	0.007	0.010	0.004	0.004
A4	0.001	0.003	0.004	0.004	0.005	0.005	0.006	0.006	0.009	0.003	0.004
A5	0.001	0.003	0.004	0.004	0.005	0.005	0.006	0.007	0.010	0.003	0.004
A6	0.001	0.004	0.005	0.005	0.006	0.007	0.008	0.008	0.012	0.004	0.006
A7	0.001	0.005	0.006	0.006	0.007	0.008	0.010	0.010	0.014	0.005	0.007
A8	0.001	0.004	0.005	0.005	0.006	0.007	0.008	0.009	0.012	0.005	0.006
A9	0.002	0.006	0.007	0.006	0.008	0.009	0.010	0.011	0.016	0.006	0.007
A10	0.002	0.008	0.010	0.010	0.012	0.013	0.016	0.016	0.024	0.009	0.011

TABLE XVII. The correlation matrix for the point-to-point uncertainties in the forward-central dijet measurements (Topology B). The relative luminosity and beam polarization uncertainties, which are common to all the data points, are not included.

Bin	B1	B2	B3	B4	B5	B6	B7	B8	B9	B10	B11
B1	1	0.013	0.010	0.011	0.008	0.010	0.008	0.008	0.006	0.006	0.005
B2		1	0.024	0.027	0.019	0.023	0.018	0.018	0.014	0.012	0.009
B3			1	0.023	0.018	0.023	0.019	0.020	0.016	0.015	0.012
B4				1	0.021	0.026	0.023	0.024	0.019	0.018	0.014
B5					1	0.022	0.020	0.021	0.017	0.016	0.013
B6						1	0.027	0.029	0.023	0.022	0.018
B7							1	0.027	0.022	0.022	0.017
B8								1	0.024	0.024	0.019
B9									1	0.020	0.016
B10										1	0.015
B11											1

TABLE XVIII. The correlation matrix for the point-to-point uncertainties coupling the forward-central dijet measurements (Topology B) with the central-central dijet measurements (Topology C). The relative luminosity and beam polarization uncertainties, which are common to all the data points, are not included.

Bin	C1	C2	C3	C4	C5	C6	C7	C8	C9	C10
B1	0.001	0.004	0.002	0.003	0.003	0.003	0.004	0.004	0.004	0.009
B2	0.002	0.007	0.005	0.007	0.007	0.006	0.009	0.009	0.007	0.018
B3	0.002	0.009	0.006	0.009	0.009	0.007	0.012	0.011	0.009	0.024
B4	0.003	0.012	0.008	0.011	0.011	0.009	0.014	0.014	0.012	0.029
B5	0.002	0.011	0.007	0.010	0.010	0.008	0.013	0.012	0.011	0.027
B6	0.003	0.015	0.010	0.014	0.014	0.011	0.018	0.017	0.015	0.038
B7	0.003	0.015	0.010	0.013	0.014	0.011	0.018	0.017	0.015	0.037
B8	0.004	0.016	0.011	0.015	0.015	0.012	0.020	0.019	0.016	0.041
B9	0.003	0.013	0.009	0.012	0.013	0.010	0.017	0.016	0.014	0.034
B10	0.003	0.013	0.009	0.012	0.012	0.010	0.016	0.015	0.013	0.033
B11	0.002	0.010	0.007	0.010	0.010	0.008	0.013	0.012	0.011	0.027

TABLE XIX. The correlation matrix for the point-to-point uncertainties coupling the forward-central dijet measurements (Topology B) with the forward-backward dijet measurements (Topology D). The relative luminosity and beam polarization uncertainties, which are common to all the data points, are not included.

Bin	D1	D2	D3	D4	D5	D6	D7	D8	D9	D10	D11
B1	0.001	0.002	0.002	0.002	0.003	0.003	0.003	0.003	0.005	0.002	0.002
B2	0.001	0.004	0.004	0.004	0.005	0.006	0.007	0.007	0.010	0.004	0.005
B3	0.001	0.005	0.006	0.005	0.007	0.007	0.009	0.009	0.013	0.005	0.006
B4	0.002	0.006	0.007	0.007	0.008	0.009	0.011	0.011	0.016	0.006	0.007
B5	0.002	0.005	0.006	0.006	0.008	0.008	0.010	0.010	0.015	0.005	0.007
B6	0.002	0.007	0.009	0.008	0.011	0.012	0.014	0.014	0.021	0.007	0.010
B7	0.002	0.007	0.009	0.008	0.010	0.012	0.014	0.014	0.020	0.007	0.009
B8	0.002	0.008	0.010	0.009	0.011	0.013	0.015	0.015	0.022	0.008	0.010
B9	0.002	0.007	0.008	0.008	0.010	0.011	0.012	0.013	0.019	0.007	0.009
B10	0.002	0.006	0.008	0.007	0.009	0.010	0.012	0.012	0.018	0.007	0.008
B11	0.002	0.005	0.006	0.006	0.008	0.008	0.010	0.010	0.015	0.005	0.007

TABLE XX. The correlation matrix for the point-to-point uncertainties in the central-central dijet measurements (Topology C). The relative luminosity and beam polarization uncertainties, which are common to all the data points, are not included.

Bin	C1	C2	C3	C4	C5	C6	C7	C8	C9	C10
C1	1	0.004	0.003	0.004	0.004	0.003	0.003	0.003	0.002	0.006
C2		1	0.016	0.018	0.017	0.012	0.016	0.013	0.011	0.024
C3			1	0.019	0.017	0.012	0.013	0.010	0.008	0.017
C4				1	0.019	0.013	0.016	0.013	0.010	0.022
C5					1	0.012	0.015	0.013	0.010	0.023
C6						1	0.012	0.010	0.008	0.018
C7							1	0.015	0.012	0.029
C8								1	0.011	0.027
C9									1	0.023
C10										1

TABLE XXI. The correlation matrix for the point-to-point uncertainties coupling the central-central dijet measurements (Topology C) with the forward-backward dijet measurements (Topology D). The relative luminosity and beam polarization uncertainties, which are common to all the data points, are not included.

Bin	D1	D2	D3	D4	D5	D6	D7	D8	D9	D10	D11
C1	0.000	0.001	0.001	0.001	0.002	0.002	0.002	0.002	0.003	0.001	0.001
C2	0.001	0.004	0.005	0.005	0.006	0.007	0.008	0.009	0.013	0.005	0.006
C3	0.001	0.003	0.004	0.004	0.004	0.005	0.006	0.006	0.009	0.003	0.004
C4	0.001	0.004	0.005	0.005	0.006	0.007	0.008	0.008	0.011	0.004	0.005
C5	0.001	0.004	0.005	0.005	0.006	0.007	0.008	0.008	0.012	0.004	0.005
C6	0.001	0.003	0.004	0.004	0.005	0.006	0.006	0.007	0.010	0.004	0.004
C7	0.002	0.006	0.007	0.006	0.008	0.009	0.010	0.011	0.016	0.006	0.007
C8	0.002	0.005	0.006	0.006	0.008	0.008	0.010	0.010	0.015	0.005	0.007
C9	0.001	0.005	0.006	0.005	0.007	0.007	0.008	0.009	0.013	0.005	0.006
C10	0.003	0.011	0.014	0.013	0.016	0.018	0.021	0.022	0.032	0.012	0.015

TABLE XXII. The correlation matrix for the point-to-point uncertainties in the forward-backward dijet measurements (Topology D). The relative luminosity and beam polarization uncertainties, which are common to all the data points, are not included.

Bin	D1	D2	D3	D4	D5	D6	D7	D8	D9	D10	D11
D1	1	0.004	0.012	0.007	0.007	0.005	0.005	0.003	0.003	0.001	0.001
D2		1	0.009	0.006	0.007	0.006	0.006	0.005	0.007	0.003	0.003
D3			1	0.014	0.015	0.012	0.011	0.008	0.010	0.004	0.004
D4				1	0.010	0.008	0.008	0.007	0.008	0.003	0.004
D5					1	0.010	0.010	0.008	0.010	0.004	0.004
D6						1	0.009	0.008	0.011	0.004	0.005
D7							1	0.009	0.012	0.005	0.006
D8								1	0.012	0.005	0.006
D9									1	0.007	0.008
D10										1	0.003
D11											1

- [1] S. Dulat, T.-J. Hou, J. Gao, M. Guzzi, J. Huston, P. Nadolsky, J. Pumplin, C. Schmidt, D. Stump, and C.-P. Yuan, *Phys. Rev. D* **93**, 033006 (2016).
- [2] Y.-B. Yang, J. Liang, Y.-J. Bi, Y. Chen, T. Draper, K.-F. Liu, and Z. Liu, *Phys. Rev. Lett.* **121**, 212001 (2018).
- [3] X. Ji, *Phys. Rev. Lett.* **74**, 1071 (1995).
- [4] B. I. Abelev *et al.* (STAR Collaboration), *Phys. Rev. Lett.* **97**, 252001 (2006).
- [5] B. I. Abelev *et al.* (STAR Collaboration), *Phys. Rev. Lett.* **100**, 232003 (2008).
- [6] L. Adamczyk *et al.* (STAR Collaboration), *Phys. Rev. D* **86**, 032006 (2012).
- [7] L. Adamczyk *et al.* (STAR Collaboration), *Phys. Rev. Lett.* **115**, 092002 (2015).
- [8] A. Adare *et al.* (PHENIX Collaboration), *Phys. Rev. D* **76**, 051106 (2007).
- [9] A. Adare *et al.* (PHENIX Collaboration), *Phys. Rev. Lett.* **103**, 012003 (2009).
- [10] A. Adare *et al.* (PHENIX Collaboration), *Phys. Rev. D* **79**, 012003 (2009).
- [11] L. Adamczyk *et al.* (STAR Collaboration), *Phys. Rev. D* **89**, 012001 (2014).
- [12] A. Adare *et al.* (PHENIX Collaboration), *Phys. Rev. D* **90**, 012007 (2014).
- [13] D. de Florian, R. Sassot, M. Stratmann, and W. Vogelsang, *Phys. Rev. Lett.* **113**, 012001 (2014).
- [14] E. R. Nocera, R. D. Ball, S. Forte, G. Ridolfi, and J. Rojo (NNPDF Collaboration), *Nucl. Phys. B* **887**, 276 (2014).
- [15] C. Bourrely and J. Soffer, *Nucl. Phys. A* **941**, 307 (2015).
- [16] N. Sato, W. Melnitchouk, S. E. Kuhn, J. J. Ethier, and A. Accardi (Jefferson Lab Angular Momentum Collaboration), *Phys. Rev. D* **93**, 074005 (2016).
- [17] Y.-B. Yang, R. S. Sufian, A. Alexandru, T. Draper, M. J. Glatzmaier, K.-F. Liu, and Y. Zhao (χ QCD Collaboration), *Phys. Rev. Lett.* **118**, 102001 (2017).
- [18] Y. V. Kovchegov, D. Pitonyak, and M. D. Sievert, *J. High Energy Phys.* **10** (2017) 198.
- [19] J. Pumplin, D. R. Stump, J. Huston, H. L. Lai, P. M. Nadolsky, and W. K. Tung, *J. High Energy Phys.* **07** (2002) 012.

- [20] A. Mukherjee and W. Vogelsang, *Phys. Rev. D* **86**, 094009 (2012).
- [21] D. de Florian, *Phys. Rev. D* **79**, 114014 (2009).
- [22] L. Adamczyk *et al.* (STAR Collaboration), *Phys. Rev. D* **95**, 071103(R) (2017).
- [23] J. Adam *et al.* (STAR Collaboration), *Phys. Rev. D* **98**, 032011 (2018).
- [24] D. de Florian, G. A. Lucero, R. Sassot, M. Stratmann, and W. Vogelsang, [arXiv:1902.10548](#).
- [25] A. Adare *et al.* (PHENIX Collaboration), *Phys. Rev. D* **93**, 011501(R) (2016).
- [26] J. Adam *et al.* (STAR Collaboration), *Phys. Rev. D* **98**, 032013 (2018).
- [27] M. Harrison, T. Ludlam, and S. Ozaki, *Nucl. Instrum. Methods Phys. Res., Sect. A* **499**, 235 (2003).
- [28] H. Hahn *et al.*, *Nucl. Instrum. Methods Phys. Res., Sect. A* **499**, 245 (2003).
- [29] I. Alekseev *et al.*, *Nucl. Instrum. Methods Phys. Res., Sect. A* **499**, 392 (2003).
- [30] O. Jinnouchi *et al.*, [arXiv:nucl-ex/0412053](#).
- [31] H. Okada *et al.*, [arXiv:hep-ex/0601001](#).
- [32] K. Ackermann *et al.*, *Nucl. Instrum. Methods Phys. Res., Sect. A* **499**, 624 (2003).
- [33] M. Anderson *et al.*, *Nucl. Instrum. Methods Phys. Res., Sect. A* **499**, 659 (2003).
- [34] M. Beddo *et al.*, *Nucl. Instrum. Methods Phys. Res., Sect. A* **499**, 725 (2003).
- [35] C. Allgower *et al.*, *Nucl. Instrum. Methods Phys. Res., Sect. A* **499**, 740 (2003).
- [36] W. J. Llope *et al.*, *Nucl. Instrum. Methods Phys. Res., Sect. A* **759**, 23 (2014).
- [37] C. Adler, A. Denisov, E. Garcia, M. Murray, H. Strobele, and S. White, *Nucl. Instrum. Methods Phys. Res., Sect. A* **470**, 488 (2001).
- [38] G. C. Blazey, J. R. Dittmann, S. D. Ellis, V. D. Elvira, K. Frame, S. Grinstein, R. Hirosky, R. Piegaia, H. Schellman, R. Snihur, V. Sorin, and D. Zeppenfeld, [arXiv:hep-ex/0005012](#).
- [39] M. Cacciari, G. P. Salam, and G. Soyez, *J. High Energy Phys.* **04** (2008) 063.
- [40] M. Cacciari, G. P. Salam, and G. Soyez, *Eur. Phys. J. C* **72**, 1896 (2012).
- [41] T. Aaltonen *et al.* (CDF Collaboration), *Phys. Rev. D* **92**, 092009 (2015).
- [42] B. Abelev *et al.* (ALICE Collaboration), *Phys. Rev. D* **91**, 112012 (2015).
- [43] S. Frixione and G. Ridolfi, *Nucl. Phys.* **B507**, 315 (1997).
- [44] T. Sjostrand, S. Mrenna, and P. Skands, *J. High Energy Phys.* **05** (2006) 026.
- [45] R. Brun, F. Bruyant, F. Carminati, S. Giani, M. Maire, A. McPherson, G. Patrick, and L. Urban, GEANT detector description and simulation tool Reports No. CERN-W5013, 1994.
- [46] P. Z. Skands, *Phys. Rev. D* **82**, 074018 (2010); [arXiv:1005.3457v5](#).
- [47] J. Adams *et al.* (STAR Collaboration), *Phys. Lett. B* **637**, 161 (2006).
- [48] G. Agakishiev *et al.* (STAR Collaboration), *Phys. Rev. Lett.* **108**, 072302 (2012).
- [49] J. K. Adkins, Studying transverse momentum dependent distributions in polarized proton collisions via azimuthal single spin asymmetries of charged pions in jets, Ph.D. thesis, University of Kentucky, 2017.
- [50] Z. Chang, Inclusive jet longitudinal double-spin asymmetry A_{LL} measurements in 510 GeV polarized pp collisions at STAR, Ph.D. thesis, Texas A&M University, 2016.
- [51] W. B. Schmidke *et al.*, RHIC polarization for runs 9-17, Brookhaven National Laboratory Report No. BNL-209057-2018-TECH, 2018.
- [52] D. Cronin-Hennessy, A. Beretvas, and P. F. Derwent, *Nucl. Instrum. Methods Phys. Res., Sect. A* **443**, 37 (2000).
- [53] L. Huo, In-jet tracking efficiency analysis for the STAR time projection chamber in polarized proton-proton collisions at $\sqrt{s} = 200$ GeV, Master's thesis, Texas A&M University, 2012.
- [54] J. Adams *et al.* (STAR Collaboration), *Phys. Rev. C* **70**, 054907 (2004).